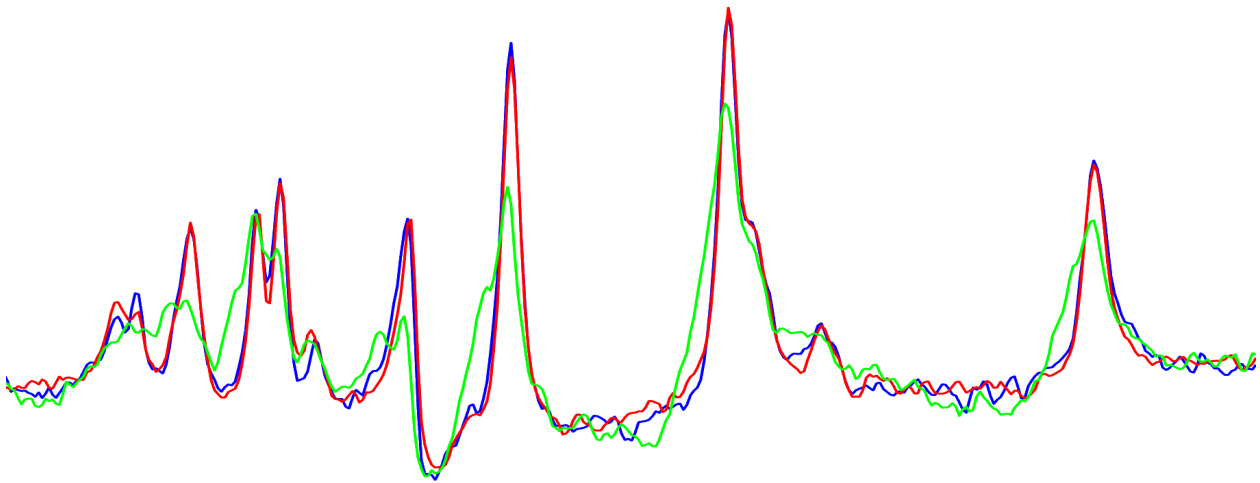


## MASTER ASSIGNMENT

# Removing barriers for lactate quantification in the portal vein using deuterium metabolic imaging



G.W.D. Wennemars

*Student Biomedical Engineering*

*High field MRI group - UMC Utrecht*

*Multi-Modality Medical Imaging group - University of Twente*

### *Examination committee*

Prof.dr. R.H. Geelkerken

Dr.ir. W. Branderhorst

Dr. W.J.M. van der Kemp

Dr.ir. W.M. Brink

Prof.dr. D.W.J. Klomp

Dr.ir. F.F.J. Simonis

March 3, 2025

# Contents

<b>Samenvatting</b>	<b>1</b>
<b>Abstract</b>	<b>2</b>
<b>List of abbreviations and terms</b>	<b>3</b>
<b>1 Introduction</b>	<b>5</b>
1.1 Background information . . . . .	8
1.1.1 Chronic mesenteric ischemia . . . . .	8
1.1.2 Magnetic resonance spectroscopy . . . . .	9
1.1.3 Quantification . . . . .	11
1.1.4 Deuterium metabolic imaging . . . . .	12
<b>2 Methods</b>	<b>13</b>
2.1 Experiment 1: In vivo MRI scans for respiratory motion, organ size and visualization . .	13
2.1.1 Population . . . . .	13
2.1.2 Setup . . . . .	13
2.1.3 Scanning . . . . .	13
2.1.4 Measuring motion . . . . .	14
2.1.5 Size measurements . . . . .	14
2.1.6 Feasibility of REST slab suppression . . . . .	14
2.2 Experiment 2: In vivo $^{31}\text{P}$ -MRSI scans for investigating the quality of spectra, spectral linewidth, SNR, and CRLB, and quantification of spectra . . . . .	15
2.2.1 Introduction . . . . .	15
2.2.2 Scanning . . . . .	15
2.2.3 Reconstruction . . . . .	17
2.2.4 Respiratory motion . . . . .	18
2.2.5 Objective 2: Investigate whether quality of spectra differs between gated acquisition with regular breathing, non-gated acquisition with regular breathing and non-gated acquisition with deep breathing in in vivo 7T $^{31}\text{P}$ -MRSI	18
2.2.6 Objective 3: Investigate whether there is a difference in spectral linewidth, SNR and CRLB between gated acquisition with regular breathing, non-gated acquisition with regular breathing and non-gated acquisition with deep breathing in in vivo 7T $^{31}\text{P}$ -MRSI . . . . .	19
2.2.7 Objective 4: Investigate whether there is an impact on the repeatability of the quantification of concentrations of homogeneously distributed liver metabolites between gated acquisition with regular breathing, non-gated acquisition with regular breathing and non-gated acquisition with deep breathing in in vivo 7T $^{31}\text{P}$ -MRSI . . . . .	19
2.3 Experiment 3: $^1\text{H}$ -MRSI at 1.5T on a phantom simulation of respiratory motion of the stomach . . . . .	20
2.3.1 Design . . . . .	20
2.3.2 Scanning . . . . .	21
2.3.3 Data processing . . . . .	22
2.3.4 Measures . . . . .	22
<b>3 Results</b>	<b>23</b>
3.1 Introduction . . . . .	23
3.2 Objective 1: Investigate the amount of motion of the liver, portal vein, stomach, diaphragm and gall bladder in regular and deep breathing by MRI . . . . .	23
3.2.1 Respiratory motion in experiment 1 . . . . .	23

3.2.2	Organ size . . . . .	26
3.3	Objective 2: Investigate whether quality of spectra differs between gated acquisition with regular breathing, non-gated acquisition with regular breathing and non-gated acquisition with deep breathing in in vivo 7T $^{31}\text{P}$ -MRSI . . . . .	26
3.4	Objective 3: Investigate whether there is a difference in spectral linewidth, SNR and CRLB between gated acquisition with regular breathing, non-gated acquisition with regular breathing and non-gated acquisition with deep breathing in in vivo 7T $^{31}\text{P}$ -MRSI . . . . .	28
3.5	Objective 4: Investigate whether there is an impact on the repeatability of the quantification of concentrations of homogeneously distributed liver metabolites between gated acquisition with regular breathing, non-gated acquisition with regular breathing and non-gated acquisition with deep breathing in in vivo 7T $^{31}\text{P}$ -MRSI . . . . .	34
3.6	Objective 5: Investigate whether the effects of ghosting can be reduced effectively with a REST slab suppressive sequence on a phantom simulation of respiratory motion of the stomach with 1.5T $^1\text{H}$ -MRSI . . . . .	35
3.6.1	Feasibility of REST slab suppression . . . . .	35
3.6.2	Phantom experiment with acetone container, scanned with $^1\text{H}$ -MRSI at 1.5T . . . . .	36
<b>4</b>	<b>Discussion</b>	<b>41</b>
4.1	Discussion of results . . . . .	41
4.1.1	Objective 1: Investigate the amount of motion of the liver, portal vein, stomach, diaphragm and gall bladder in regular and deep breathing by MRI . . . . .	41
4.1.2	Objective 2: Investigate whether quality of spectra differs between gated acquisition with regular breathing, non-gated acquisition with regular breathing and non-gated acquisition with deep breathing in in vivo 7T $^{31}\text{P}$ -MRSI . . . . .	42
4.1.3	Objective 3: Investigate whether there is a difference in spectral linewidth, SNR and CRLB between gated acquisition with regular breathing, non-gated acquisition with regular breathing and non-gated acquisition with deep breathing in in vivo 7T $^{31}\text{P}$ -MRSI . . . . .	42
4.1.4	Objective 4: Investigate whether there is an impact on the repeatability of the quantification of concentrations of homogeneously distributed liver metabolites between gated acquisition with regular breathing, non-gated acquisition with regular breathing and non-gated acquisition with deep breathing in in vivo 7T $^{31}\text{P}$ -MRSI . . . . .	43
4.1.5	Objective 5: Investigate whether the effects of ghosting can be reduced effectively with a REST slab suppressive sequence on a phantom simulation of respiratory motion of the stomach with 1.5T $^1\text{H}$ -MRSI . . . . .	44
4.2	Experimental discussion . . . . .	44
4.2.1	Experiment 1: In vivo MRI scans at 1.5T for respiratory motion, organ size and visualization . . . . .	44
4.2.2	Experiment 2: In vivo $^{31}\text{P}$ -MRSI scans for investigating the quality of spectra, spectral linewidth, SNR, and CRLB, and quantification of spectra . . . . .	45
4.2.3	Experiment 3: $^1\text{H}$ -MRSI at 1.5T on a phantom simulation of respiratory motion of the stomach . . . . .	47
4.3	General discussion . . . . .	51
4.3.1	General remark regarding objective 2, 3 and 4 (In vivo 7T $^{31}\text{P}$ -MRSI) . . . . .	51
4.3.2	General remark regarding objective 5 (Phantom simulation of ghosting) . . . . .	51
4.3.3	Implications for current practice . . . . .	51
4.3.4	Future developments for $^2\text{H}$ -MRSI as an accessible function test for CMI . . . . .	51
<b>5</b>	<b>Conclusion</b>	<b>54</b>
<b>A</b>	<b>Additional results</b>	<b>59</b>
A.1	Similarity of in vivo $^{31}\text{P}$ -MRSI to literature [39] . . . . .	60
A.2	Location of subselection of voxels in experiment 2 . . . . .	61

<b>B</b>	<b>Lists</b>	<b>62</b>
B.1	List of Figures . . . . .	62
B.2	List of Tables . . . . .	66

# Samenvatting

## Introductie

Chronische mesenterische ischemie (CMI) wordt veroorzaakt door verminderde mesenterische bloedtoevoer. De diagnose wordt bemoeilijkt door aspecifieke symptomen en grote anatomische variatie. Detectie van lactaat via  $^2H$ -MRSI in de poortader zou als functietest kunnen werken, maar kan beïnvloed worden door ademhalingsbeweging. Deze studie evalueert de huidige praktijk van niet-gegateerde acquisitie en onderzoekt de impact hiervan op spectrale kwaliteit, lijnbreedte, signaal-ruisverhouding, Cramér-Rao-ongelijkheden en de herhaalbaarheid van kwantificatie. Daarnaast wordt door de maag geïnduceerde ghosting gesimuleerd en onderdrukt in een fantoomstudie.

## Methode

De ademhalingsbeweging van de poortader, galblaas en maag werd gemeten bij drie vrijwilligers met 1,5T MRI. De impact van ademhalingsbewegingen op spectra werd onderzocht in de lever met behulp van  $^{31}P$ -MRSI met 7T. Gegateerde vrije ademhaling, niet-gegateerde vrije ademhaling en niet-gegateerde diepe ademhaling werden vergeleken. Ghosting werd onderzocht met een fantoomexperiment waarbij een bewegende acetoncontainer als surrogaat voor de maag werd gebruikt, geanalyseerd met  $^1H$ -MRSI met 1,5T.

## Resultaten

Alle onderzochte structuren vertoonden vergelijkbare ademhalingsbewegingen. Er werd geen duidelijk verschil gevonden tussen gegateerde en niet-gegateerde vrije ademhaling. Niet-gegateerde diepe ademhaling presteerde in alle aspecten consequent slechter. Ghosting-artifacten werden succesvol gesimuleerd en onderdrukt met een REST-slab suppressiesequentie.

## Impact

Deze studie vond geen bewijs dat niet-gegateerde acquisitie lever-MRSI negatief beïnvloedt bij vrije ademhaling. Bovendien lijkt vermindering van ghosting haalbaar. Verder onderzoek is nodig naar in hoeverre deze bevindingen ook gelden voor  $^2H$ -MRSI in de poortader.

# Abstract

## Introduction

Chronic mesenteric ischemia (CMI) results from reduced mesenteric blood flow. Its diagnosis is challenged by nonspecific symptoms and large morphological variability. Detecting lactate via  $^2\text{H}$ -MRSI in the portal vein could serve as a function test but may be affected by respiratory motion. This study evaluates the current practice of non-gated acquisition, assessing its impact on spectral quality, linewidth (LW), signal-to-noise ratio (SNR), Cramér-Rao Lower Bounds (CRLB) and repeatability of quantification. Moreover, stomach-induced ghosting is simulated and suppressed in a phantom study.

## Methods

Respiratory motion of the portal vein, gall bladder and stomach was measured in 3 volunteers at 1.5T MRI. The impact of respiratory motion on spectra was investigated in the liver using  $^{31}\text{P}$ -MRSI at 7T. Gated free breathing, non-gated free breathing and non-gated deep breathing scans were compared. Ghosting was investigated using a phantom simulation with a moving acetone container as surrogate for the stomach using  $^1\text{H}$ -MRSI at 1.5T.

## Results

All investigated structures had similar respiratory motion. No clear difference was found between gated and non-gated free breathing acquisition. Non-gated deep breathing consistently performed worse in every aspect. Ghosting artifacts were successfully simulated and suppressed with a REST slab suppressive sequence.

## Impact

This study found no evidence that non-gated acquisition negatively affects liver MRSI in free breathing. Moreover, ghosting reduction appears feasible. Further research is required to confirm the applicability of these findings for  $^2\text{H}$ -MRSI in the portal vein.

## List of abbreviations and terms

**Table 1:** All abbreviations used in this thesis.

Term	Definition
AMARES	advanced method for accurate, robust, and efficient spectral fitting
AMI	acute mesenteric ischemia
AoCMI	acute on chronic mesenteric ischemia
AP	anterior to posterior direction (front to back of body)
ATP	adenosine triphosphate
$B_0$	permanent magnetic field
$B_1$	RF pulse used for excitation
CA	celiac artery
CMI	chronic mesenteric ischemia
CR	coefficient of repeatability
CRLB	Cramér-Rao lower bound
DICOM	Digital Imaging and Communications in Medicine, standard file format for MRI scans
DMI	deuterium metabolic imaging ( $=^2H$ -MRSI)
ER	endovascular revascularization
FFE	fast field echo (Philips' implementation of a gradient echo)
FH	feet to head direction
FOV	field-of-view
FWHM	full-width-half-maximum
$G_F$	gated free breathing
GPC	glycerophosphocholine
GPE	glycerophosphoethanolamine
IMA	inferior mesenteric artery
LW	linewidth
MAL	median arcuate ligament
MALS	median arcuate ligament syndrome
MR	magnetic resonance
MRI	magnetic resonance imaging
MRSI	magnetic resonance spectroscopic imaging
MVT	mesenteric venous thrombosis
NADH	nicotinamide adenine dinucleotide
$NG_D$	non-gated deep breathing
$NG_F$	non-gated free breathing
NMR	nuclear magnetic resonance
NOMI	non-occlusive mesenteric ischemia
OSMAR	open surgical mesenteric artery revascularization
PC	phosphocholine
PCA	principal component analysis
PCr	phosphocreatine
PDE	phosphodiester
PE	phosphoethanolamine
Pi	inorganic phosphate
PME	phosphomonoester
ppm	parts per million, unit of chemical shift
PSF	point spread function
PtdC	phosphatidylcholine
REST	REgional Saturation Technique

**Table 1:** All abbreviations used in this thesis.

Term	Definition
RF	radio frequency
RL	right to left direction
SMA	superior mesenteric artery
SNR	signal-to-noise-ratio
SVS	single voxel spectroscopy
T	tesla (unit of magnetic field strength)
$T_1$	longitudinal relaxation time
$T_2$	transversal relaxation time
$T_E$	echo time
$T_R$	repetition time
UDPG	uridine diphosphate glucose
VLS	visual light spectroscopy

# 1 Introduction

Chronic mesenteric ischemia (CMI) [1] is a disease where there is a shortage of oxygen in the intestinal tissue. CMI is a relatively rare disease that affects about 9.2/100.000 people [2]. CMI can cause severe complaints [1, 3], such as post-prandial pain, a fear of eating, weight loss, nausea and vomiting. Moreover, it can progress into acute-on-chronic mesenteric ischemia (AoCMI [4]), which has a high mortality rate [4]. AMI, or acute mesenteric ischemia can also happen without a chronic stage. In one study [5], the 90-day mortality rate for patients with AMI was 83%. If AMI occurs, symptoms develop in minutes to hours, and can have a very high mortality rate if untreated within a matter of hours [6]. The main clinical symptom for AMI is severe abdominal pain.

CMI can be characterized as occlusive mesenteric ischaemia or non-occlusive mesenteric ischaemia (NOMI). Occlusive chronic mesenteric ischaemia is most often caused by stenoses in the mesenteric arteries due to atherosclerosis [1]. NOMI is often caused by other diseases, such as anaemia, shock or low cardiac output. [7]

In healthy people, the tip of the villi in the intestines is susceptible to ischemia [8]. If blood is needed elsewhere, the blood flow to the intestines can be reduced, leading to reversible ischemia in the villi [9]. In people with mesenteric ischemia, a larger part of the villi becomes ischemic.

In chronic cases, the blood flow is sufficient for the energy requirement in rest. In acute cases, blood flow is insufficient even in rest. This may start a chain reaction of processes, leading to necrosis and eventually to peritonitis, which is often fatal [10].

The symptoms of CMI are nonspecific, challenging diagnosis. The classic symptoms of CMI are postprandial symptoms, such as nausea and a niggling, brick-like or balloon-like feeling, weight loss, and abdominal bruit. The presence of the combination of all these symptoms is only about 60% predictive of CMI [1].

Diagnosis of CMI is further challenged by a weak correlation between anatomical variations and prevalence of the disease. This is because there are many collateral pathways between the mesenteric arteries. If there is a restriction in one of the mesenteric arteries, the blood flow to the intestines can often be maintained by increased flow in the collaterals [4]. Generally [1], CMI is considered likely if there are symptoms appropriate to and significant stenoses in the coeliac artery (CA) and superior mesenteric artery (SMA). However, if only 1 of these arteries has a stenosis, the probability of CMI is lower. Treating these patients for CMI may lead to overtreatment.

Generally, duplex ultrasound is used as a first screening method [4]. Computed tomography angiography (CTA) or magnetic resonance angiography (MRA) are recommended to image stenoses, as well as an upper gastrointestinal endoscopy [1]. The gold standard [1] for diagnosis, retrospectively, is a relief of symptoms after revascularization.

The previously described techniques rely on characterizing and identifying stenoses. However, as mentioned, the presence of one or more stenoses in the mesenteric arteries does not always indicate the presence of CMI and vice versa. Moreover, symptoms are also not a reliable method of diagnosing CMI. Therefore, functional tests that directly show the ischemia itself are essential.

Some of the previously developed function tests [1] are visual light spectroscopy (VLS), which shows ischemia by directly measuring oxygen saturation, and tonometry, which measures carbon dioxide pressure, which increases in ischemia [11]. These tests were all invasive, next to various other downsides [1]. A current field of research is that of blood markers, but this has not yet yielded a definitively effective marker for diagnosis [1, 12].

A non-invasive technique that has the potential to be used as a function test is magnetic resonance spectroscopic imaging (MRSI). The end goal of this thesis is to contribute to the development of this function test.

In MRSI, metabolites can be detected based on differences in resonance frequencies in the presence of a magnetic field, see section 1.1.2. MRSI could be used to show ischemia by measuring elevated lactate concentration in the portal vein. Lactate is a product of anaerobic glycolysis, by which the intestines generate energy without sufficient oxygen supply. All blood that has passed any part of the

intestines will go through the portal vein to the liver, where it is further processed [13]. As a result, the lactate concentration in the portal vein should increase in ischemia, regardless of which part of the intestines is exactly ischemic. Therefore, this function test should be able to show ischemia, regardless of the exact type of ischemia, morphology and symptoms. The non-invasiveness is the largest advantage of MRSI over tonometry, while the ability to detect ischemia regardless of the exact spatial variation is an additional large advantage over VLS.

In previous studies,  $^1\text{H}$ -MRSI was studied, which yields spectra of metabolites which contain protons. The main challenge with this, is separating the signal from lactate from the much more abundant signal from lipids [14–17].

An alternative approach is the use of  $^2\text{H}$ -MRSI, or deuterium metabolic imaging (DMI) [18]. This yields spectra of metabolites containing deuterium ( $^2\text{H}$ ), an isotope of hydrogen containing both a proton and a neutron, as opposed to  $^1\text{H}$  which only consists of a proton. The natural abundance of  $^2\text{H}$  is low [18], and spectra are sparse with little overlap between peaks.

In  $^2\text{H}$ -MRSI, the subject is given  $^2\text{H}$ -glucose, which is, in case of mesenteric ischemia, metabolised to  $^2\text{H}$ -lactate in the intestines through the aforementioned anaerobic glycolysis. This yields spectra in which  $^2\text{H}$ -lactate peaks are clearly visible and not overshadowed by peaks of lipids or other substances.

In MRSI, subject motion is a process known to worsen acquired spectra in several ways [19], such as increased linewidths (LW) in spectra, reduction in signal to noise ratio's (SNR)[20], and incorrect quantification [21]. Moreover, due to tissue shifting across voxels, a spectrum of a voxel may actually be (partially) generated by a different area than expected. The structures in the abdomen are subject to respiratory motion. This could affect quantitative  $^2\text{H}$ -MRSI measurements in the portal vein. Preliminary results suggest that respiratory motion strongly impacts the linewidth of spectra [22]. It is therefore plausible that MRSI spectra in the portal vein will also be negatively affected by respiratory motion. In ongoing  $^2\text{H}$ -MRSI studies in the liver, artifacts have been observed that are attributed to the ghosting artifact, which is an artifact that can be induced by periodic motion, see Fig 1 For a short explanation, please see Section 1.1.2.7. In this case, it is attributed to the motion of the stomach due to respiration, which contains a lot of signal due to the ingested  $^2\text{H}$ -glucose. To minimize the effects of ghosting, only 2 of the 8 available coils are used in reconstruction of this data. It is expected that  $^2\text{H}$ -MRSI studies on the portal vein will be affected in a very similar way. Resolving this tissue would allow for the use of more data in reconstruction and better spectra in  $^2\text{H}$ -MRSI.

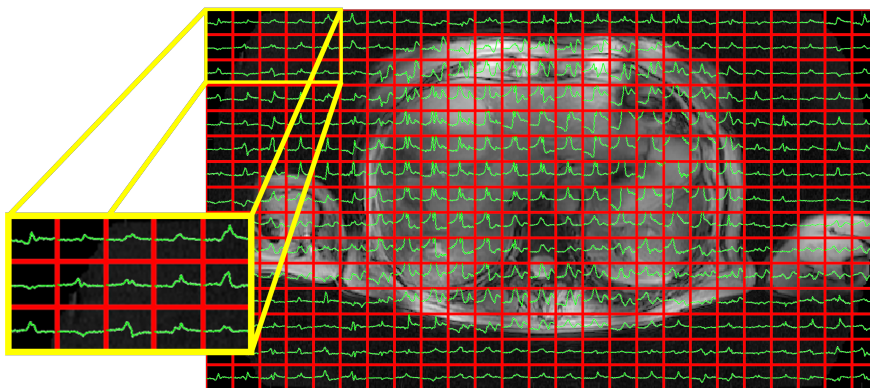


**Figure 1:** An example of suspected ghosting in a  $^2\text{H}$ -MRSI study. It can be seen that signal is reconstructed in several areas outside of the body. Courtesy of Jeanine Prompers, UMC Utrecht.

Investigating the influence of respiratory motion on  $^2\text{H}$ -MRSI is very important. Firstly, because the portal vein may be especially sensitive to respiratory motion due to its small size. Secondly, because the accuracy of the quantification of lactate concentration is very important. As mentioned, some ischemia in the liver can be completely healthy. Therefore, some level of lactate may always be detected and accurate detection of an elevated pathological concentration is very important.

Quantification is often done by comparing the signal intensity of a certain peak to the total fitted signal or the signal of a specific different peak, and therefore it is important that there is no contamination through ghosting by  $^2H$ -glucose.

The aforementioned effects of respiratory motion can be decreased by performing respiratory-gated acquisition. However, respiratory gating greatly increases the already long MRSI scans [23] and is therefore not commonly used.

This thesis aims to elucidate what kind of effects can be expected due to respiratory motion as a result of performing these non-gated acquisitions in  $^2H$ -MRSI of the portal vein.

This thesis investigates several of the mentioned effects of respiratory motion in MRSI. Subjectively, the effect of respiratory motion on the quality of spectra is investigated by visually judging the distinctiveness of peaks in several ways. Objectively, the effect of respiratory motion on several parameters commonly used to judge spectral quality, such as LW, SNR and Cramér-Rao Lower Bounds (CRLB) (Section 1.1.3.2), is determined. CRLB's are expected to increase in lower quality spectra, as accurate determination of metabolite concentrations will be challenged. Moreover, the effect of respiratory motion on the quantification of metabolites using AMARES (Section 1.1.3.1) is researched. The ghosting artifact found in  $^2H$ -MRSI studies is reproduced in a phantom and the suitability of a REST slab suppressive sequence (Section 1.1.2.8) to reduce this artifact is investigated.

In vivo MRSI experiments in this thesis are performed using  $^{31}P$ -MRSI on the liver, as performing  $^2H$ -MRSI on the portal vein was not possible. To administer  $^2H$  to volunteers, it was required to go through the process of ethical approval, which was not possible in the project time frame. An important distinction of this substitution is that the liver and the portal vein are of a different size. As a result, the metabolite content of a voxel in the liver will likely change less due to a different tissue moving into the voxel due to respiratory motion than in the portal vein. Recent developments [24–26] have made it possible to perform  $^{31}P$ -MRSI measurements on organs that are deep in the abdomen, like the liver.

In vivo MRI experiments are performed to measure the motion of abdominal organs as a result of regular and deep breathing. The first primary use of this information is to verify whether abdominal organs are subject to similar respiratory motion, which is needed to support the substitution of portal vein MRSI with liver MRSI. The second primary goal is to use the amplitude of respiratory motion is needed to design a phantom experiment with realistic motion.

The first secondary use of this information is to investigate whether all parts of the portal vein are subject to similar respiratory motion, in order to see if effects of respiratory motion on portal vein MRSI may be reduced by scanning a different part of the portal vein. Using the same data, the sizes of the portal vein and gall bladder are measured in order to see if gall bladder MRSI measurements may be a more accurate substitute for portal vein MRSI than liver MRSI. Moreover, the imaging data is used to create a visualization on whether a REST slab suppressive sequence can be implemented in a way that the portal vein is not affected.

Concretely, the main objectives of this study are as follows:

1. Investigate the amount of motion of the liver, portal vein, stomach, diaphragm and gall bladder in regular and deep breathing by MRI.
2. Investigate whether quality of spectra differs between gated acquisition with regular breathing, non-gated acquisition with regular breathing and non-gated acquisition with deep breathing in in vivo  $^{31}P$ -MRSI.
3. Investigate whether there is a difference in spectral linewidth, SNR and CRLB between gated acquisition with regular breathing, non-gated acquisition with regular breathing and non-gated acquisition with deep breathing in in vivo  $^{31}P$ -MRSI.
4. Investigate whether there is an impact on the repeatability of the quantification of concentrations of homogeneously distributed liver metabolites between gated acquisition with regular breathing, non-gated acquisition with regular breathing and non-gated acquisition with deep breathing in in vivo  $^{31}P$ -MRSI.

5. Investigate whether the effects of ghosting can be reduced effectively with a REST slab suppressive sequence on a phantom simulation of respiratory motion of the stomach with 1.5T  $^1H$ -MRSI.

## 1.1 Background information

The aim of the background section is to serve as a glossary for information that is important for understanding the disease context and to provide short explanations of terminology and techniques.

### 1.1.1 Chronic mesenteric ischemia

#### Anatomy

The anatomy of the mesenteric circulation is shown in Fig. 2. There is a large variation in anatomy between patients [1]. The connected network of collaterals protects the gut against ischemia.

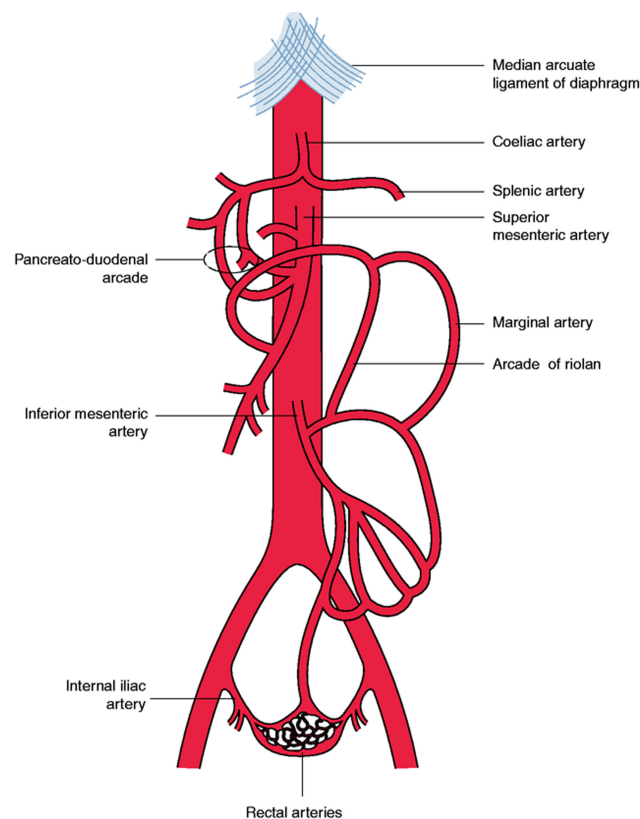


**Figure 2:** The anatomy of the arterial mesenteric circulation [1]. The coeliac artery (CA) perfuses liver, spleen, pancreas, stomach and part of the duodenum. The superior mesenteric artery (SMA) perfuses part of the duodenum, the jejunum, ileum, ascending colon and the largest part of the transverse colon. The inferior mesenteric artery (IMA) perfuses the rest of the transverse colon, the descending colon, sigmoid and rectum. These three arteries are connected by a large network of collaterals.

#### Cause of symptoms

After eating, the oxygen requirement of the intestines increases [1]. The mesenteric blood flow increases by up to 30-150%. In patients with chronic mesenteric ischemia, this demand cannot be matched, causing the post-prandial pain.

#### Causes

The main causes of CMI have already been highlighted in the introduction. Occlusive CMI [1] is mainly caused by atherosclerosis. Atherosclerosis is more prevalent in females and is related to aging [27]. Some risk factors [1] for chronic mesenteric ischemia caused by atherosclerosis are smoking, hypertension, diabetes, high cholesterol and a (family) history of cardiovascular disease.

Other suggested causes [1] of occlusive CMI are median arcuate ligament syndrome (MALS), vasculitis and mesenteric venous thrombosis (MVT). MALS is a controversial cause of occlusive CMI. The hypothesis is that the median arcuate ligament (MAL) can compress the CA, especially during maximal expiration. Vasculitis is a group of uncommon conditions that are related to inflammation of blood vessels [28]. MVT [1] is a very rare cause. It can cause AMI due to obstruction of the mesenteric circulation.

### **Treatment**

The treatment for CMI is revascularization. Open surgical mesenteric artery revascularization (OSMAR) has been replaced by endovascular revascularization (ER). ER is the recommended procedure, and OSMAR is recommended to be reserved for patients in whom ER is not suitable [1].

## **1.1.2 Magnetic resonance spectroscopy**

### **1.1.2.1 Magnetic resonance**

Magnetic resonance spectroscopic imaging (MRSI) is based on the principles of magnetic resonance (MR). In MR scanners, a permanent magnetic field  $B_0$  is present, directed along the bore. The net magnetization [29] of nuclei with a spin in the subject will align with this magnetic field. The individual nuclei precess around  $B_0$  with a nucleus-specific resonance frequency, determined by their nucleus-specific gyromagnetic ratio. By applying a second magnetic field  $B_1$  rotating with this frequency via a radiofrequency (RF) pulse, the net magnetization can be tipped perpendicular to  $B_0$ . The magnetization, precessing around  $B_0$  after it has been tipped, induces a current in coils in the scanner, which is the measured signal. Depending on its molecular environment, a nucleus can experience a slightly different  $B_0$  and thus have a slightly different resonance frequency. By Fourier transforming the acquired MR signal, the individual contributions of nuclei with different resonance frequencies are evaluated. This is the spectrum that is used in MR spectroscopy.

Depending on the molecular environment of a nucleus, it can experience a slightly different  $B_0$  field [30]. This results in a slightly different resonance frequency and a slightly different measured frequency. By applying a Fourier transform to the MR signal acquired in the coils, the individual contributions of nuclei with different resonance frequencies are evaluated. This is the spectrum that is used in MR spectroscopy.

### **1.1.2.2 Shimming**

The permanent magnetic field  $B_0$  is generally generated by a superconducting magnet. The magnetic field is not completely homogeneous due to the finite length of the magnet and small errors in fabrication. To correct these inhomogeneities, additional magnets are installed in the scanner. These generate additional magnetic fields which correct the deviations in the main magnetic field as good as possible [30].

### **1.1.2.3 Spatial encoding**

Performing the previous steps yields the signal for the entire volume. However, to perform MR spectroscopic imaging, it is needed to reconstruct the signal to different spatial locations. In MRSI, this is generally done using a process called phase encoding.

In phase encoding [30], an additional magnetic field, on top of  $B_0$  is applied for a short time to the volume using gradient coils. This shortly gives all the spins in the volume a different resonance frequency, as they experience a different magnetic field. If the gradient is turned off, their resonance frequency will be the same again. However, they will have accumulated a slightly different phase as a result of the different frequency for a short time. This varying phase influences the signal that is acquired. The gradients can be turned on in all directions, giving the spins up to 3 accumulated phases.

If no gradient is applied, the contributions of individual particles to the net magnetization are in phase and the measured signal is maximal. If the gradient strength is varied, the phase varies across the sample, with a frequency related to the gradient strength, a spatial frequency. The signal is acquired at various gradient strengths, each time yielding a signal for a new spatial frequency. These signals

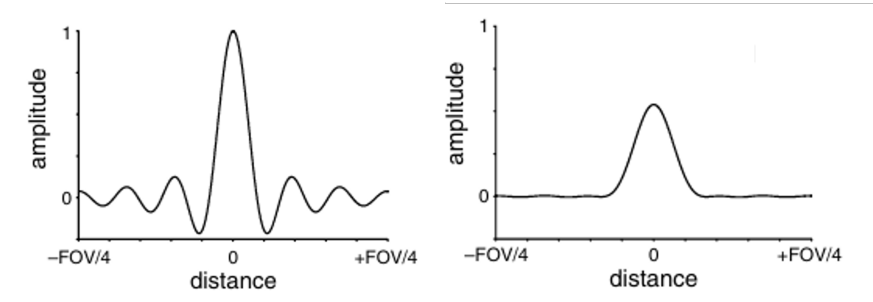


**Figure 3:** Left: a typical PSF. Note the side lobes, decreasing in height, that represent the signal spreading to neighbouring voxels. Right: The effect of a Hamming filter on the PSF. Notice that the main lobe is wider and lower, and that the sidelobes have almost disappeared. Modified from [30].

are stored in k-t-space [31]. For 3D MRSI, this is a 4-dimensional space. 3 dimensions describe the spatial frequency that is created using the gradients. The 4th dimension contains the full signal that is acquired in each of these phase encoding steps. Fourier transforming the 3 spatial dimensions for every slice in the time dimension yields an 'image' for every measured time point. A second Fourier transform is applied along the time axis, over these images, to obtain localized spectra.

#### 1.1.2.4 Motion reduction

Phase encoding is a slow process, where, in conventional MRSI, only 1 spatial frequency can be measured per  $T_R$ , the repetition time. The repetition time is the time between two excitations. As a result, MRSI scans take a lot of time. The in vivo  $^{31}\text{P}$ -MRSI scans at 7T performed in this thesis for example, would take 35 minutes if Hamming weighted (Section 1.1.2.6) acquisition was not applied. It is not possible to acquire a similar 3D encoded scan within 1 breath hold. A method to reduce breathing motion in a MRI scan is to use respiratory-gated acquisition [32]. That means that data is acquired only during either the exhale or inhale state. However, this greatly increases scan time.

#### 1.1.2.5 Point spread function

The voxel size in MRSI is determined by the size of the total field of view (FOV) and the number of phase encoding steps [30]. However, in practice, the signal that is reconstructed in a voxel also contains signal from surrounding voxels. This is due to the Fourier transformation. To yield perfectly localised signal after Fourier transformation, an infinite number of phase encoding steps is needed. However, as only a finite measurement is possible, it is not possible to sample a perfect voxel. In Fig. 3, the shape of a realistic PSF can be seen. The side lobes of this PSF are where signal is reconstructed that is supposed to be in the voxel.

#### 1.1.2.6 Hamming filtering

It is possible to reduce negative PSF effects by applying certain filters [30], such as a Hamming or Hann filter. A Hamming filter reduces the side lobes at the cost of a broader main peak. So, the PSF has much less effects on a larger distance, but the effective voxel size increases. A Hamming filter reduces the signal of high-frequency k-space coordinations. Applying it after acquisition several averages of a full k-space is very inefficient. It is also possible to implement the Hamming filter at acquisition already, by acquiring fewer high frequency k-space points. The time saved with this can be used for a shorter scan time, or for additional acquisitions of lower frequency k-space points.

#### 1.1.2.7 Ghosting

Ghosting is an artifact caused by motion of the subject during phase encoding. Ghosting is well described in MR imaging (MRI). If the motion is periodic, the PSF will become a structure with a maximum at the actual position and ghosts along the phase encoding direction in 2D images with 1 phase encoding direction [33]. In 1D MRSI, it was found that ghost artifacts behave the same way as in MRI [34]. In 2D and 3D MRSI, this is also expected [33]. Ghosting can be reduced by increasing the number of averages or performing respiratory gating [33].

### 1.1.2.8 Spatial saturation

To reduce signal coming from outside a volume of interest, spatial saturation pulses can be used. These selectively excite a volume that is not of interest, so that there is very little magnetization left when the actual volume of interest is excited. Therefore, the amount of signal that is coming from the saturated region is reduced strongly [35]. An implementation of this type of sequence for Philips scanners, that is used in this thesis, is called a REST slab (REgional Saturation Technique).

### 1.1.3 Quantification

Exact direct quantification [30] from a signal to an absolute concentration is not possible, because this requires exact knowledge of several environmental factors. It is possible to quantify metabolite concentrations by comparing the signal of a metabolite to the signal of a reference compound. However, this is still quite complex. In practice, metabolite ratios are often used. However, metabolite ratios are less reliable than absolute concentrations, because ratios can be impacted in more ways. A change in a metabolite ratio, for example, can be caused by a change in concentration of either, or both of the involved metabolites. Moreover, the signal can be influenced by other things than the concentration, such as changed relaxation parameters.

#### 1.1.3.1 AMARES

A common method to quantify spectra, and the method used in this thesis, is AMARES (advanced method for accurate, robust and efficient spectral fitting). The full details of AMARES are described in [36]. AMARES minimizes the difference between the fit and the signal using a nonlinear least squares algorithm [37]. The model that AMARES attempts to fit can be customized to use specific prior knowledge and to fit Lorentzian or Gaussian lineshapes for peaks. The prior knowledge [36] can contain many things, such as information about multiplets, known ratios and individual phases.

#### 1.1.3.2 Objective measures of spectral quality

Some popular objective measures for spectral quality [38], that will be used in this thesis, are the signal-to-noise ratio (SNR), linewidth (LW) and Cramér-Rao Lower Bounds (CRLB).

##### SNR

The signal-to-noise ratio can be defined in several ways, but is always defined by a ratio of some definition of a signal and some definition of noise. In a spectrum, it could be defined as the height of the highest [38] or a specific [39] peak divided by the standard deviation of the signal in an area where no peaks are expected. In the time domain signal [38], before a Fourier transform is performed, it could be defined as the signal amplitude at time zero, when the signal has minimally dephased, divided by the noise at the end of the acquisition, when the signal has maximally dephased. SNR is proportional to the size of the region of interest and proportional to the square root of the number of averaged acquisitions.

##### Linewidth

Linewidth [38] is a measure of the width of a certain peak. It is often defined by the full-width-half-maximum (FWHM), which is the width of a peak at half of the maximum height of the peak. The linewidth determines the resolution with which peaks can be differentiated from each other. Large linewidths are associated with worse model fitting and larger CRLB [38].

The inherent minimum linewidth [40] is determined by the transverse relaxation time  $T_2$  and differences in magnetic susceptibility in tissue structure. The linewidth may be larger than this as a result of  $B_0$  inhomogeneities or poor  $B_0$  shimming. Shimming is the process by which the  $B_0$  field is homogenized as much as possible by use of additional gradient coils. It may not be possible to correct for all inhomogeneities using available shimming. Furthermore, it can be increased by other effects, such as eddy currents or fluctuations between averages.

##### Cramér-Rao Lower Bounds

Cramér-Rao Lower Bounds (CRLB) are an estimate of the lower limit of the fitting error, and not the actual quality of the fit. They describe the inherent error in a model with certain parameters. The CRLB is not a direct measure of the fitting error and may be over- or underestimated from the true

CRLB if the used fitting model and parameters are incorrect or if there are any systematic errors. Generally, CRLB's decrease with increased SNR, and increase with increased LW [38].

#### 1.1.4 Deuterium metabolic imaging

Deuterium metabolic imaging (DMI), or, as it will be referred to in this thesis,  $^2H$ -MRSI, is a type of MRSI which measures deuterium-containing compounds. Other available MRSI techniques have several drawbacks, that DMI does not have.

$^1H$ -MRSI [41] is challenged by difficulties surrounding suppression of water and lipids. These are compounds present in the human body in very high concentrations, which will influence the signal. Moreover, the excitation of  $^1H$ -MRSI requires short wavelengths as it has a high gyromagnetic ratio. The gold standard for measuring metabolic pathways is  $^{13}C$ -MRSI. The main difficulty of this type of  $^{13}C$ -MRSI is that its sensitivity low and its complexity is high. Methods to increase the sensitivity are technically challenging and expensive.

$^2H$  is an isotope of hydrogen which contains both a neutron and a proton, as opposed to  $^1H$ , which contains just a proton.  $^2H$  has a much lower Larmor frequency than  $^1H$  and short relaxation times [41]. The lower frequency means that the wavelengths needed for excitation are longer. As a result, there are no issues with standing wave effects at high field strengths. The short relaxation times allow for faster averaging and higher sensitivity. Moreover, compared to  $^1H$ -MRSI,  $^2H$ -MRSI is less sensitive to magnetic field inhomogeneity.

$^2H$  has a low natural abundance. In vivo, the natural abundance is about 0.02% [42]. As a result, the background signal is very low. The natural abundance of deuterated water is measurable, as is, depending on the tissue, some natural abundance lipids. This is a benefit over  $^{13}C$ , as the natural abundance of 1.1 % leads to large lipid signals [41].

Finally,  $^2H$ -MRSI is a simple method compared to other types of MRSI. Because of the low background signal, water or lipid suppression techniques are not required [41].

## 2 Methods

### 2.1 Experiment 1: In vivo MRI scans for respiratory motion, organ size and visualization

Objective 1, regarding the measurement of typical motion of liver, portal vein, stomach, diaphragm and gall bladder, and the secondary objectives of determination of the size of the gall bladder and portal vein and visualization of possible placement of a REST slab suppressive scan were performed on the same dataset of in vivo 1.5T MRI scans obtained of three volunteers.

#### 2.1.1 Population

The volunteer population is described in table 2.

**Table 2:** The population of the volunteers for the in vivo motion and organ size measurements.

Sex	Age
2 M / 1 V	20, 23, 26

#### 2.1.2 Setup

The experiments were performed on 1.5T (Philips, Best, The Netherlands). An abdominal coil was used for reception, placed on the thorax. The experimental setup can be seen in Fig. 4



**Figure 4:** The experimental setup for experiment 1 at the 1.5T scanner with a volunteer out of the bore. The abdominal coil is placed on the thorax. The volunteer was positioned feet first.

#### 2.1.3 Scanning

The used scan settings are tabulated in Table 3. Volunteers were given instructions to either breathe normally or breathe deeply. All scans were performed twice, once when the volunteer was breathing regularly and once when the volunteer was breathing deeply.

**Table 3:** The scan settings used for scanning the volunteers. For FOV, voxel size and # voxels, the numbers represent respectively the AP, RL, FH direction. All scans are a balanced FFE scan. The precise echo and repetition time vary slightly between scan protocols, likely due to automatic optimization by the scanner. The transversal scan was not used for motion measurements, as no full cycle could be seen of any marked structure as motion was primarily perpendicular to the scan plane.

Scan settings	Slices	FOV (mm)	$T_R$ (ms)	$T_E$ (ms)	Voxel size (mm)	# voxels	# frames
Coronal	5	50*499.5*499.5	~3.2	~1.6	10*1.95*1.95	1*256*256	50
	1	10*499.5*499.5	~3.2	~1.6	10*1.95*1.95	1*256*256	200
Transversal scan, oriented parallel to portal vein	1	499.5*499.5*10	~3.2	~1.6	1.95*1.95*10	256*256*1	20
Sagittal	1	499.5*10*499.5	~3.2	~1.6	1.95*10*1.95	256*1*256	20

#### 2.1.4 Measuring motion

Typical respiratory motion was determined by manually marking specific structures on several MR scans through the respiratory cycle. For this purpose, a custom Python 3.12 [43] script was developed. In this script, the specific structures were manually marked. Then, the distance between the upper and lower boundaries of the projection of the organ onto the 3-D spatial x-, y- and z-axes was outputted. The voxel size, saved in the DICOM header, was used to convert this to distances.

##### Marked structures

Motion was measured at five points at different recognizable structures. Three of these were marked in the coronal view. These were any recognizable structure in the portal vein near the hilum, any recognizable structure in the portal vein near the spine and the most superior part of the stomach at the diaphragm. Two were marked in the sagittal view. These were the portal vein and gall bladder. The gall bladder was often not visible in a coronal view, and its motion in feet-head direction could still be compared to the portal vein using this marking. The marked points can be seen in Fig. 9.

#### 2.1.5 Size measurements

For performing size measurements, the 'Opened curve' tool of MicroDicom (MicroDicom Ltd, Sofia, Bulgaria) was used. This reports a distance in pixel units. As the pixel size was equal in the displayed directions, direct manual conversion of pixels to mm was possible.

The measurements were made on scans where the volunteers breathed freely, without any instructions. For each structure, a slice was used where the structure was well visible. So, different slices may be used for portal vein and gall bladder measurements.

##### Marked structures

The length of the portal vein was measured from the branch to the most medial end of the portal vein. This was possible in two of the three scanned volunteers. In the third, there was no visible branching into two large vessels. Therefore, for this volunteer, the length was taken from the medial end to the part where the vein branched in many smaller vessels. The diameter of the portal vein was measured at multiple locations in the unbranched part of the portal vein in the coronal plane and once in the sagittal plane.

The gall bladder was measured along its shortest and longest axis in any plane where it was well visible.

#### 2.1.6 Feasibility of REST slab suppression

The feasibility of REST slab suppression is investigated by seeing if anatomically, it is possible to position the REST slab in a way that the portal vein is not affected.

To do this, the shape of the portal vein and liver was drawn in transversal scans performed as described in section 2.1.3. In these scans, a profile of the suppressed slice in REST slab suppression was drawn. The orientation of the REST slab in the phantom experiment (Experiment 3) was based on the results of

the motion determination. For this visualization, it was assumed that the sequences are performing perfectly and only within their target regions. This is not completely realistic, as in reality there are always imperfections, such as  $B_0$  inhomogeneities and PSF effects. This experiment therefore only served as a proof-of-principle visualization of the situation, to see if there was any potential in investigating the sequences further in the phantom experiment (Experiment 3).

## 2.2 Experiment 2: In vivo $^{31}\text{P}$ -MRSI scans for investigating the quality of spectra, spectral linewidth, SNR, and CRLB, and quantification of spectra

Objectives 2-4, regarding respiratory gating and deep breathing and their impact on quality, linewidth, SNR, CRLB and quantified concentrations were investigated using in vivo  $^{31}\text{P}$ -MRSI at 7T on six volunteers.

### 2.2.1 Introduction

The data processing for the in vivo  $^{31}\text{P}$ -MRSI data was as similar as possible to the data processing performed in [39]. This thesis has been made with a very similar setup. The main difference was that a different  $B_1$  coil was used. The goal of replicating the method as much as possible was to be able to compare any results as good as possible to literature, especially results of objective 4 (repeatability of quantification).

### 2.2.2 Scanning

Scans were performed on a 7T scanner (Philips, Best, The Netherlands). An in-house developed double-tuned  $^{31}\text{P}$  and  $^2\text{H}$  receive coil was used with integrated  $^1\text{H}$  transceivers. If applicable, respiratory gating was applied using a respiratory belt sensor (Invivo Corporation, Orlando, Florida, U.S.A.). The experimental setup can be seen in Fig. 5.



**Figure 5:** Measurement setup of in vivo MRSI scans at 7T. The coils were placed below and on top of the thorax. The air bag of the respiratory sensor was placed on the stomach using a belt. The respiratory sensor itself was placed between the legs. Volunteers were positioned feet first.

The characteristics of the volunteer population are tabulated in Table 4. Six volunteers were scanned, because this was considered to be the minimum sample size for significant conclusions.

**Table 4:** The characteristics of the volunteer population for the  $^{31}\text{P}$ -MRSI scans.

Sex	Age
2 M / 4 F	22,23,23,24,26,44

The performed  $^{31}\text{P}$ -MRSI scans are tabulated in Table 5. Reference images were acquired in the

following respiratory states: free breathing exhale, free breathing inhale and box breathing inhale. If required, free breathing exhale images were assumed to be representative of box breathing exhale states. The box breathing scans were introduced later in the project, as very few differences were found between the gated and non-gated free breathing scan. Therefore, box breathing scans are only acquired of volunteers V3-V6.

Two reference MRI videos were acquired in the coronal plane, one with free breathing and one with box breathing instruction.

**Table 5:** Acquired  $^{31}\text{P}$ -MRSI scans. The values for FOV and Voxel size represent respectively AP, RL, FH. For the  $^{31}\text{P}$ -MRSI scans, Hamming weighted acquisition was acquired with ten averages. The deep breathing scans were implemented later in time, which is why these were only acquired for 4 volunteers.

Type	$T_R$ (ms)	$T_E$ (ms)	FOV (mm)	Voxel size (mm)	Instruction	Gating	# samples	Dynamics
$^{31}\text{P}$ -MRSI	60	0.5	300*500*340	20*20*20	None	Yes	6	-
$^{31}\text{P}$ -MRSI	60	0.5	300*500*340	20*20*20	None	No	6	-
$^{31}\text{P}$ -MRSI	60	0.5	300*500*340	20*20*20	Box	No	4	-
FFE	4.0	0.99	10*480*320	10*5*5	None	No	6	200
FFE	4.0	0.99	10*480*320	10*5*5	Box	No	4	550

The box breathing pattern was meant to simulate a worst-case-scenario of free breathing. It consisted of four phases: a five second inhale, a five second hold, a five second exhale, a five second hold. See Fig. 6. To one of the four volunteers (V3), the pattern was communicated via sound of the Calm app (Calm, San Francisco, California, U.S.A.). To three of the four volunteers (V4, V5, V6), it was communicated via a projection of colors, as the sound of the app could be difficult to hear over the scanner sound. It is not expected to have had a negative effect, because the volunteer V3 was able to follow the pattern. In the remainder of the thesis, this scan will be referred to as deep breathing, unless the method itself is meant.

The idea behind the deep breathing scan is to show two things. First, it can show if an investigated parameter is ever expected to change as a result of respiratory motion. If it does not change in the deep breathing scan, it should also not be affected by not performing respiratory gating in a free breathing volunteer. Second, it can show if a lack of differences between a gated and non-gated free breathing scan could be due to experimental mistakes. If there are no differences in a certain parameter between the free breathing scans with and without respiratory gating, but there is a large difference in a parameter in the deep breathing scan, the lack of differences can be due to the fact that non-gating does not affect the data enough.

The goal is not to investigate the exact relationship between the amount of respiratory motion and spectral worsening in this thesis.

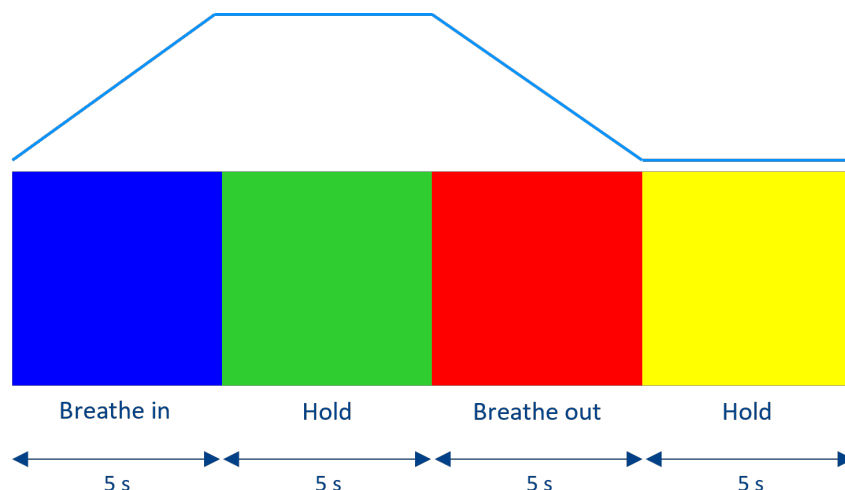


**Figure 6:** Schematic overview of the box breathing pattern used to guide the subject in performing a consistent deep breathing pattern. Color guidance was used for three of the four subjects and an audio signal for one of the four subjects.

Reference images were acquired in the following respiratory states: free breathing exhale, free breathing inhale and box breathing inhale. If required, free breathing exhale images were assumed to be representative of box breathing exhale states.

Two reference videos were acquired in the coronal plane, one with free breathing and one with box breathing instruction.

### 2.2.3 Reconstruction

The data was reconstructed from the scanner in .list/.data format. This data was processed using a modified version of the DEplete-pipeline developed in-house. The DEplete package has been used in other publications [44]. The modifications made were either to accomplish the methods described in this section, or to improve user interaction efficiency, especially related to processing multiple datasets. The exact reconstruction of the spectra differed for the different objectives. It will be described which reconstruction is used for which steps later.

First, the data was averaged over all acquisitions. Then, a Hamming correction is applied. Then, the spectra were phased per channel by minimizing the imaginary part of the point with the maximum absolute signal value for every channel.

Two reconstructions were performed. In the first reconstruction, no denoising was performed. In the second reconstruction, principal component analysis-based (PCA) denoising [45] was performed. Afterwards, in both reconstructions, the channels were decorrelated using Cholesky decomposition. Then, Roemer channel combination was used [46]. Depending on the objective, one of the two reconstructions is used.

### Fitting

AMARES was used to fit metabolite concentrations and to obtain linewidth values for spectra. To fit concentrations at the right location, AMARES needed a reference point in the signal. Moreover, a reference point was needed to phase the spectra. The reference point for both of these processes was the  $\alpha$ -ATP peak. By default, the  $\alpha$ -ATP peak was assumed to be the highest value within the search window of -5 to -10 ppm. During scanning of volunteer V5, due to technical difficulties, an incorrect offset (used to optimize the excitation efficiency for PCr, a metabolite that is roughly in the center of the spectrum of interest) was used which shifted all acquired spectra. This resulted in the  $\alpha$ -ATP peak laying outside of the search window for many spectra. For this volunteer, the search window was adapted to -2.5 to -10 ppm. The expected effect of the incorrect offset on the excitation efficiency for the metabolites of interest in this thesis was negligible.

Individual metabolite concentrations were expressed as a percentage of the total fitted metabolite concentrations, in the same way as the reference article [39].

CRLB's were expressed relatively, as a percentage of the individual metabolite concentrations before these were normalized to a percentage of the total fitted metabolite concentrations.

A prior knowledge file optimized for the liver was used, which was also used in previous liver studies [44]. In linewidth analyses of the liver, it was found that the linewidth, which was confined to be identical for all metabolites and should be between 20 and 90, was often limited by the upper boundary. In this thesis, this restraint has been loosened to [20,Inf] for all analyses where AMARES was used.

### Masking

A liver mask was created to reduce sensitivity to muscle and gall bladder influences on the spectra via the method reported in [39]. This mask was created based on the reconstruction without denoising of the gated free breathing scan. Voxels were removed if the fitted PCr concentration, and/or the fitted PtdC concentration was higher than the fitted  $\alpha$ -ATP concentration.

#### 2.2.4 Respiratory motion

The highest possible part of the diaphragm on the right side of the subject was tracked in the FFE scans with the same pipeline as in the 1.5T motion measurements (Experiment 1), see Section 2.1.4. This information was useful as an estimate for liver and gall bladder motion in the same volunteer of which MRSI scans were performed.

#### 2.2.5 Objective 2: Investigate whether quality of spectra differs between gated acquisition with regular breathing, non-gated acquisition with regular breathing and non-gated acquisition with deep breathing in in vivo 7T $^{31}$ P-MRSI

Due to the time-consuming process, only one volunteer was investigated.

All voxels were inspected in the unfiltered liver of volunteer V3. This volunteer was chosen, as their breathing motion amplitude in deep breathing was the largest, see Table 8. Therefore, if there was any motion-induced effect on spectral quality, it was most likely observed in this volunteer out of all volunteers.

The data was reconstructed with PCA-denoising and the judgments were performed on apodized spectra. The mask was not applied; the unfiltered liver was used with all reconstructed spectra. The spectra were investigated by eye and judged subjectively based on the distinctiveness of peaks. They were judged on three criteria.

- The first was the distinctiveness of peaks in the total spectrum. A spectrum was considered of low quality if peaks of high concentration metabolites, such as  $\gamma$ -ATP, are difficult to distinguish. If it would be difficult to recognize the peaks if the ppm axis was removed from the spectrum, the spectrum was of low quality.
- The second was the distinctiveness of the  $\gamma$ -ATP peak. This is a peak that is generally one of the clearest in the spectra. If this peak was not clearly identifiable, it was judged as low quality.
- The third was the distinctiveness of the PME and PDE peaks. These peaks generally have a relatively low intensity in the spectrum and consist of smaller peaks that are close together. When this region showed very little structure, it was judged as low quality.

For an example of a spectrum that shows on which peaks are focused in the various criteria, please see Fig. 7.

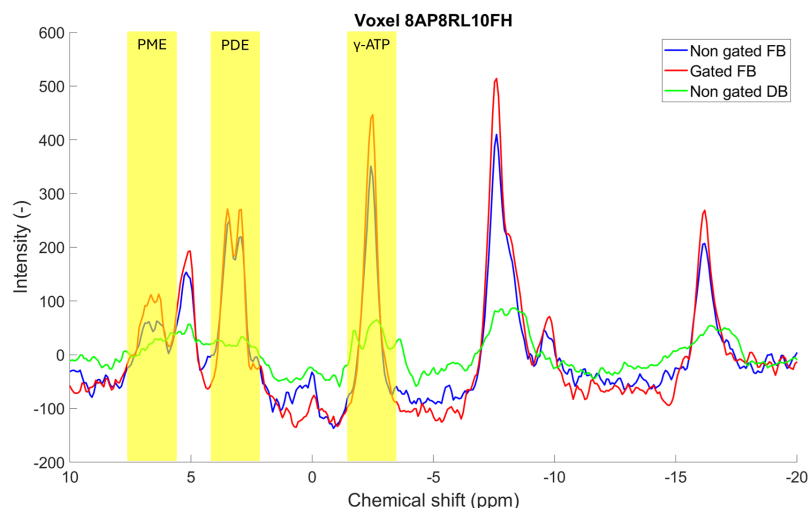


**Figure 7:** Example of a spectrum with visually distinctive peaks in the free breathing spectra and no distinctive peaks in the deep breathing spectra. These spectra are shifted based on the  $\alpha$ -ATP peak. In this example, the free breathing (FB) spectra are of acceptable quality based on every mentioned criterion, whereas the deep breathing spectrum (DB) is of low quality in every mentioned criterion.

### 2.2.6 Objective 3: Investigate whether there is a difference in spectral linewidth, SNR and CRLB between gated acquisition with regular breathing, non-gated acquisition with regular breathing and non-gated acquisition with deep breathing in in vivo $7T$ $^{31}P$ -MRSI

The data used was reconstructed with PCA-denoising. The filtered liver mask was used.

The linewidth was reported from AMARES and was fixed for all metabolites.

SNR was defined as the height of the  $\alpha$ -ATP peak divided by the sample standard deviation of the noise. The height of the  $\alpha$ -ATP peak was determined as the maximum value between -5 and -10 ppm, after shifting of the x-axis by the offset described in section 2.2.3. For calculation of the noise, the signal between 10 and 20 ppm with the shifted x-axis was used.

For CRLB, the CRLB of  $\alpha$ -ATP was used. CRLB was reported by AMARES for every metabolite.  $\alpha$ -ATP was chosen because it was found to have both a relatively high concentration and a relatively low variation across the liver compared to other metabolites in this data.

Linewidth, SNR and CRLB are reported as average per volunteer with standard deviation. This shows whether the average value changes. However, if there are both decreases and increases within the volume, their individual effects are dampened.

Therefore, histograms are shown in which the distributions of all the differences in value per voxel are shown.

In the CRLB histograms, the average and standard deviation of the differences was calculated for differences with an absolute value  $\leq 100\%$ , to limit the influence of outliers. In the linewidth and SNR histograms, all values were considered.

### 2.2.7 Objective 4: Investigate whether there is an impact on the repeatability of the quantification of concentrations of homogeneously distributed liver metabolites between gated acquisition with regular breathing, non-gated acquisition with regular breathing and non-gated acquisition with deep breathing in in vivo $7T$ $^{31}P$ -MRSI

The influence of (non)-gated acquisition on quantified concentrations was studied by investigating repeatability parameters. If the changed variable between two acquisitions does not influence the quantification, the repeatability parameters should show a result that is similar to a comparison of two identical scans. The repeatability parameters from this thesis are compared to [39], which contains repeatability parameters of two identical scans. The data of this article has been acquired with a very similar measurement setup. The only known difference between the two setups was that [39] used

an older  $B_1$  coil, which had a lower strength. The old  $B_1$  coil was  $6 \mu T$  whereas the coil of this work was  $10 \mu T$ . The data processing steps described in [39] were replicated as closely as possible.

The studied parameters were the coefficient of repeatability (CR) and bias. These are properties that are used in Bland-Altman analyses [47], which are not completely performed in this thesis.

The coefficient of repeatability (CR) is defined in equation 2. The signed differences are the differences between the average fitted metabolite value between two scans of all volunteers, see 1. One CR was obtained for every metabolite. CR describes the 95% confidence interval for the signed differences. For the small sample sizes in this thesis or in [39], the factor 1.96 does not reflect the 95% confidence interval, which will be wider. The 95% confidence interval of a distribution would be determined using a factor from the student's t-table, which would be larger than 1.96 for small sample sizes [47].

It was decided to use the same methodology and formula for CR as [39]. While it may not be reliable in interpretation as a confidence interval, the comparison may still be valuable in describing differences between the repeatability of gated and non-gated free breathing scans and the repeatability of free breathing and deep breathing scans.

The bias was defined as the average value of the signed differences, as previously described. See equation 3.

$$\text{signed difference}_i = \bar{X}_i - \bar{Y}_i \quad (1)$$

$$CR = 1.96 \cdot \text{std}(\text{signed differences}) \quad (2)$$

$$\text{Bias} = \text{average}(\text{signed differences}) \quad (3)$$

where:

- $\bar{X}_i$  is the average metabolite value for a specific acquisition  $X$  for volunteer  $i$
- $\bar{Y}_i$  is the average metabolite value for a specific acquisition  $Y$  for volunteer  $i$
- $\text{signed difference}_i$  is the difference for volunteer  $i$
- all  $\text{signed difference}_i$  are concatenated in the variable  $\text{signed differences}$
- CR is the coefficient of repeatability
- std is the sample standard deviation

### 2.3 Experiment 3: $^1H$ -MRSI at 1.5T on a phantom simulation of respiratory motion of the stomach

The goal of this experiment was to answer objective 5. Objective 5 was to investigate whether the effects of ghosting can be reduced effectively with a REST slab suppressive sequence on a phantom simulation of respiratory motion of the stomach.

The experiment had two main aims:

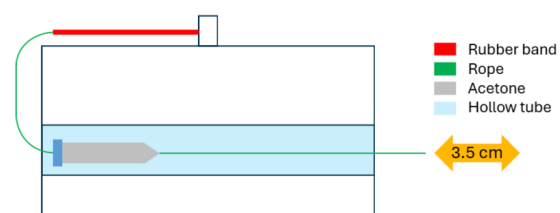
- Investigate the effects of the moving acetone container on voxels that did not contain any signal generating material
- Investigate the effectiveness of a REST slab suppressive sequence in reducing these effects

#### 2.3.1 Design

The phantom consisted of a large container with a tube through the container. Through this tube, a 50mL acetone container, connected to the box via a rubber band, was moved by hand over a certain distance over a period of eight seconds. For timing, the Soundcorset app (unknown developer) was used. The distance was based on the in vivo respiratory motion measurements (Objective 1,

experiment 1) to represent the motion of the stomach in deep breathing, a worst case scenario. Scans were performed on a 1.5T scanner (Philips, Best, The Netherlands). Two abdominal coils were used, one was placed below the phantom and one was placed on top of the phantom.

The experimental setup can be seen in Fig. 8a,8b.



**(a)** Schematic overview of a slice through the experimental setup. The distance was based on the results of the determination of typical respiratory motion in experiment 1.



**(b)** Image of the setup of an experiment very similar to the described experiment. There is no image of the experiment described in this thesis. The water syringe (bottom left) was not present in the actual experiment and the box was placed in the middle of the table, instead of to the side. During measurements, sand bags were placed against the phantom to prevent it from being moved by the pulling force on the acetone container. Moreover, the top abdominal coil (vertical in this picture) was placed on top of the phantom.

**Figure 8:** Overviews of the setup for the phantom experiment to simulate ghosting and investigate the reduction of ghosting via a REST slab suppressive sequence.

### 2.3.2 Scanning

A total of four scans were performed. In this experiment, two scan protocols were used for two scans each: a protocol without any suppression or selection, that excites the whole volume, and a REST slab suppressive protocol. The first protocol will generally be referred to in this thesis as 'non-suppressive', the second protocol as 'REST slab suppressive'. For each protocol, a scan was performed with stationary acetone container and with a moving acetone container. In this thesis, a scan with stationary acetone container will generally be referred to as *no-motion* scan, while a scan with moving acetone container will generally be referred to as *motion* scan.

The scan settings are tabulated in Table 6. The  $T_R$  is slightly different from both scans, but was expected to only lead to minor differences in signal intensities, as both  $T_R$ 's are much smaller than the  $T_1$  relaxation time, which is expected to be multiple seconds [48]. Therefore, the values were expected to be in the same order of magnitude and roughly comparable.

**Table 6:** Scan settings of the phantom experiment. The  $T_R$  is different between the two scans. Both scans are  $^1H$ -MRSI scans.

Type	FOV (AP*RL*FH) (mm)	Grid	Voxel size	$T_R$ (ms)	$T_E$ (ms)
Non-suppressive	300*220*300	15*11*15	20*20*20	100	0.5
REST slab suppressive	300*220*300	15*11*15	20*20*20	120	0.5

### 2.3.3 Data processing

The data was exported from the scanner in .SPAR/.SDAT format. A Hann window was applied to the data to reduce effects of the point spread function (PSF). A Hann window works similar to the Hamming window, see Section 1.1.2.6. The spectra were loaded into 3DiCSI [49]. Then, all voxels were selected and all spectra were exported as a .txt file. This file was used for data processing. The spectra were analyzed using Python 3.12 [43]. The maximum value present in the absolute spectra were identified for every voxel and used for quantitative analyses.

### 2.3.4 Measures

#### Signal intensity

The signal intensity in a voxel was taken as the maximum value present in its absolute spectrum.

#### Voxel selection

It was found that there was a clear signal in every voxel, even if the acetone container was stationary. Therefore, it was not possible to investigate the influence of motion voxels that contained pure noise. Moreover, the signal intensity, in the voxels that were not expected to contain signal, varied across the volume. Therefore, it was decided not to analyze a specific spatial location, but instead analyze the 10% voxels with the lowest signal intensity in the *no-motion* scan. These voxels were the most noise-like, and any influence of motion was expected to be the clearest in these voxels. For a discussion on the origin of the residual signal and the choice of 10%, please see Section 4.2.3.7.

#### Total summed signal ratio

The amount of signal increase due to ghosting was quantified by determining the summed signal intensities of the voxel selection of both the *no-motion* and *motion* scans, and dividing them to get the total summed signal ratio, see Eq. 4. It represents the average increase or decrease in signal from the *no-motion* scan to the *motion* scan in the voxel selection. Significance was not calculated, as each voxel does not represent an independent measurement due to the PSF.

$$\text{Ratio} = \frac{\sum \text{Signal}_{\text{motion}}}{\sum \text{Signal}_{\text{no-motion}}} \quad (4)$$

## 3 Results

### 3.1 Introduction

The results will be presented per experiment and per objective.

First, the results of the supporting experiments regarding in vivo measurements of morphology and respiratory motion are presented (Objective 1). Then, the in vivo MRSI experiments are presented (Objective 2-4). Finally, the phantom experiment (Objective 5) is presented.

The measurements of respiratory motion in the in vivo MRSI experiments are reported under objective 1.

### 3.2 Objective 1: Investigate the amount of motion of the liver, portal vein, stomach, diaphragm and gall bladder in regular and deep breathing by MRI

#### 3.2.1 Respiratory motion in experiment 1

##### Literature

The movements of the portal vein and gall bladder are expected to be similar to movement of the liver, as these are all located next to each other. The motion of the liver is expected [50] to be 1-2 cm in free breathing and 4-5 cm in deep breathing. The motion of the stomach is expected to be similar to that of the liver. It is expected to be in the range of 1-2 cm for free breathing [50, 51].

##### Experiment 1

The results obtained from MRI at 1.5T are tabulated in Table 7 and displayed visually in Fig. 9. It can be seen that the measured movement of the portal vein is similar in coronal and transversal measurements in shared axes. The gall bladder and portal vein move similar amounts in transversal measurements, compared in feet-head direction, the main direction of movement. The portal vein and stomach, marked at the diaphragm, move similar amounts in coronal measurements. The portal vein in free breathing moves about the same at the hilus as near the spine. The portal vein at the spine moves about the same amount in deep breathing as in free breathing. All other measured structures move a lot more in deep breathing.

Summarized, all structures have similar respiratory motion in feet-head direction in free breathing. All structures, except for the proximal part of the portal vein, near the spine, have similar respiratory motion in feet-head direction in deep breathing.

##### Experiment 2

For all the volunteers scanned for objectives 2-4, the respiratory motion is measured as well by MRI at 7T.

The respiratory motion in feet-head direction of the scanned volunteers has been measured and tabulated in Table 8. There is a large variation in respiratory motion between volunteers. Moreover, the deep breathing motion amplitude of some volunteers is smaller than the free breathing motion amplitude of others.

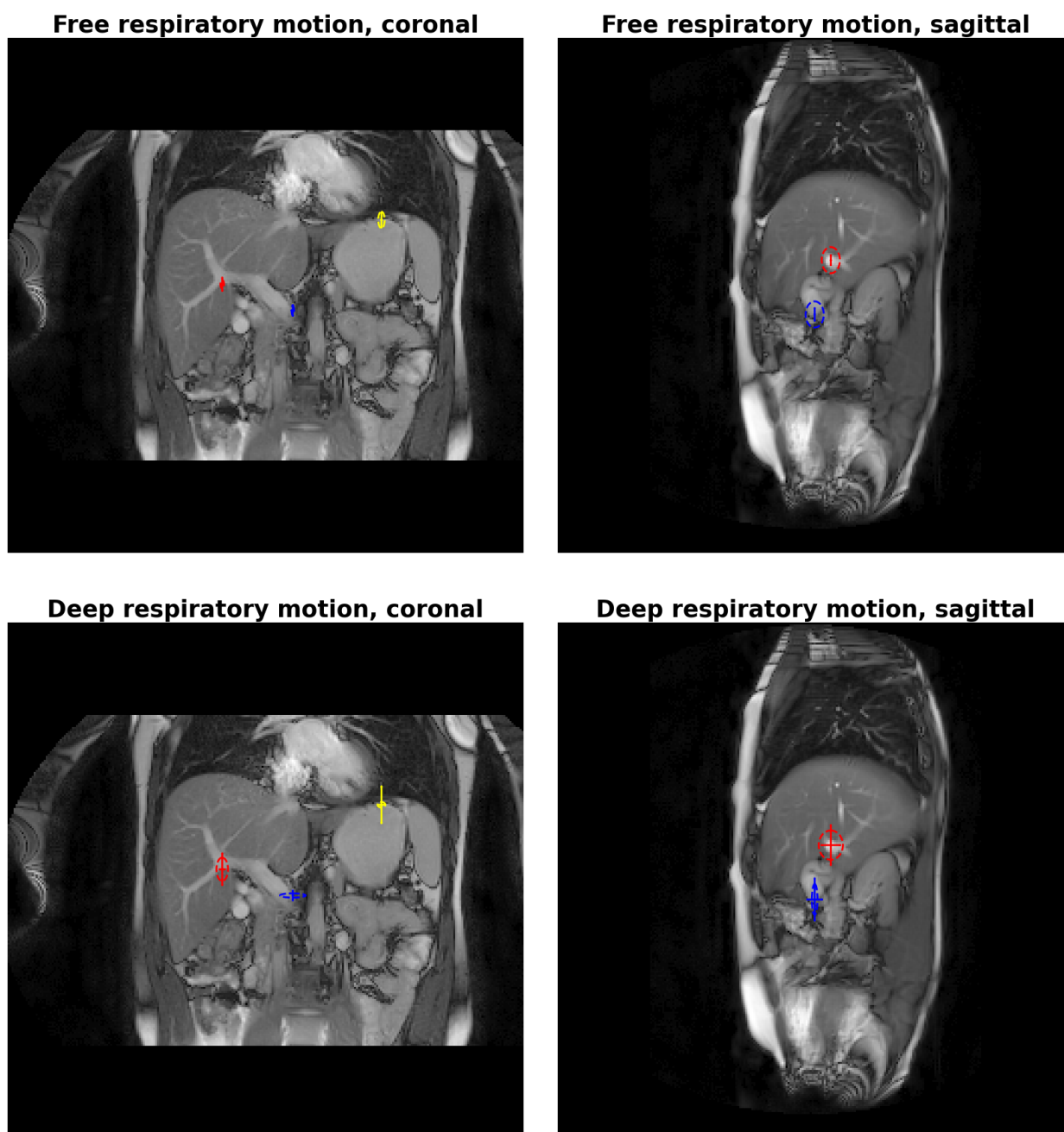


**Figure 9:** Visualization of free and deep respiration made with MRI at 1.5T. The arrows represent the movement along one axis, averaged over 3 volunteers, in free breathing. The striped line represents an ellipse with, along the axes, a radius of twice the standard deviation of the movement. The values that describe these arrows and ellipses are tabulated in Table 7. The background scans are of a free breathing volunteer, chosen because the structures are well defined in the imaged slices.

Left: coronal views. Here, the portal vein is marked at the hilus (red) and near the spine (blue). Moreover, the top of the stomach, at the diaphragm, is marked (yellow). Right: Sagittal views. Here, the portal vein (red) and gall bladder (blue) are marked. Top: Free breathing. Bottom: Deep breathing. These figures show that, visually, in free breathing, all marked structures have similar feet-head motion. In deep breathing, the structures also have similar respiratory motion, visually, except for the portal vein near the hilus. This structure is subject to less motion.

**Table 7:** Difference between maximum and minimum marked point during MRI scans at 1.5 of respiration. AP = anterior-posterior direction, LR = left-right direction, FH = feet-head direction. The portal vein in deep breathing in the coronal view was often not visible within the same plane due to imperfect plane positioning, so these values may be an underestimation of the actual respiratory motion. Any part of the portal vein that was visible in these views was marked if the target structure was not visible. As a result, LR movement may be overestimated for the portal vein in the coronal view in deep breathing. For the motion measurement of the stomach at the diaphragm, the focus was on measuring the feet-head motion at the most superior part. Therefore, the LR motion may be less accurate. The marked free breathing structures all have similar motion, as the maximum difference between the averages is 5 mm between the stomach and portal vein in the sagittal view. In deep breathing, the structures also have similar respiratory motion, except for the portal vein near the hilus, as the maximum difference in amplitude between the other structures is 10.2 mm.

			Movement per direction (mm)		
	Tracked point		AP	LR	FH
Free breathing	Portal vein (sagittal plane)	Mean	7.8		17.4
		Standard deviation	7.8		10.2
	Portal vein (coronal view)	Mean	3.3	7.4	20.5
		Standard deviation	5.8	1.8	4.2
	Gall bladder	Mean	8.2		20.0
		Standard deviation	8.8		12.7
	Portal vein near spine	Mean		6.0	18.1
		Standard deviation		1.1	4.9
	Stomach / diaphragm	Mean		8.3	22.5
		Standard deviation		3.1	8.0
Deep breathing	Portal vein (sagittal plane)	Mean	25.8		46.4
		Standard deviation	11.7		14.2
	Portal vein (coronal view)	Mean	10.0	12.9	38.3
		Standard deviation	0	5.6	11.3
	Gall bladder	Mean	22.1		48.5
		Standard deviation	2.7		15.0
	Portal vein near spine	Mean	6.7	8.2	17.1
		Standard deviation	5.8	12.4	2.1
	Stomach / diaphragm	Mean		14.7	43.3
		Standard deviation		3.8	2.6

**Table 8:** Measured free breathing and deep breathing in the volunteers scanned for in vivo MRSI at 7T. Motion is measured as the maximum difference in FH locations of the diaphragm. It can be seen that in most volunteers, the motion of the diaphragm is much larger in deep breathing than in free breathing, as expected. V1 had very a very similar amount of motion in both free breathing and deep breathing. For V1, the deep breathing amplitude is similar to the other volunteers, but the free breathing amplitude is quite large. There is quite a large variation in observed breathing amplitudes. Generally, the determined breathing motion for the diaphragm in these measurements is larger than the determined breathing motion in the 1.5T MRI measurements (Table 7).

	FH amplitude (mm)	
	Free breathing	Deep breathing
V1	48	50
V2	18	53
V3	33	82
V4	30	67
V5	40	51
V6	16	33
Mean $\pm$ std	31 $\pm$ 12	56 $\pm$ 17

### 3.2.2 Organ size

Literature values for the length of the portal vein from the start to the beginning of the branches vary from 50 [52] to 80 [53] mm. The diameter is expected to be about 10 mm [52].

Literature values for the size of the gall bladder are 5-12 cm for length and 3-5 cm for the width [54]. There are also variations in position and shape [54, 55].

The length of the visible part of the portal vein was found to be 75 mm (std: 7.5 mm). The diameter of the portal vein was found to be about 11 mm (std: 1.8 mm).

The gall bladder was diverse in presence. It had a long shape in two volunteers, of which it was not visible in a coronal plane in one. In one volunteer, it had a more circular or stumped shape. The length of a long-shaped gall bladder was found to be at most 5.3 cm with a minimum width of about 1.5 cm. The more circular gall bladder had a diameter of about 3-5 cm.

The measurements for the portal vein and gall bladder are similar to literature.

### 3.3 Objective 2: Investigate whether quality of spectra differs between gated acquisition with regular breathing, non-gated acquisition with regular breathing and non-gated acquisition with deep breathing in in vivo 7T $^{31}P$ -MRSI

In the gated acquisition, 97.7% of spectra were judged to have clear peaks. In the non-gated free breathing acquisition, this number was the same. In the non-gated deep breathing acquisition, 56.3% was found to have clear peaks. That means that almost all spectra were visually clear in the free breathing scans, and only a little more than half of the spectra were visually clear in the deep breathing scan.

The table with the manual judgements per voxel is shown in Appendix A.

**Table 9:** The percentage of spectra judged as low quality for every criterion in the 3 datasets of V3.

% judged as clear	Overall spectrum	PME & PDE peaks	$\gamma$ -ATP peak
Gated, Free breathing	97.7	93.1	98.3
Non-gated, Free breathing	97.7	90.8	98.9
Non-gated, Deep breathing	56.3	38.5	63.8

The locations of the voxels of which the overall spectrum was judged as low quality are inspected in

the free breathing scans, and completely or partially contain lung or heart tissue for a portion of the respiratory cycle. See Fig. 10

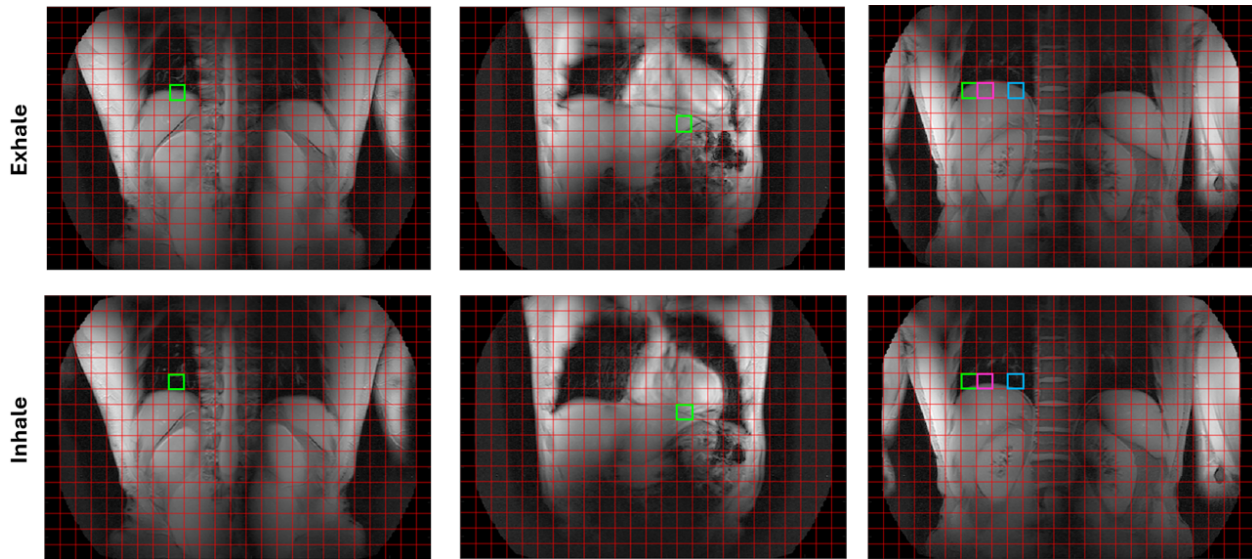


**Figure 10:** The voxels that were marked as having spectra with poorly distinguishable peaks. Green voxels were marked in both the gated and non-gated free breathing scan. The pink voxel was only marked in the non-gated free breathing scan. The blue voxel was only marked in the gated free breathing scan. It can be seen that all of these voxels are located at the border of the liver. These voxels are more likely to have large differences in their contents due to motion, expectedly leading to worse spectra.

The locations of the voxels in which the overall spectrum was judged as low quality in the deep breathing scan are shown in Fig. 11. The unclear voxels are mostly situated near the head and posteriorly. These voxels may be influenced by the lungs.

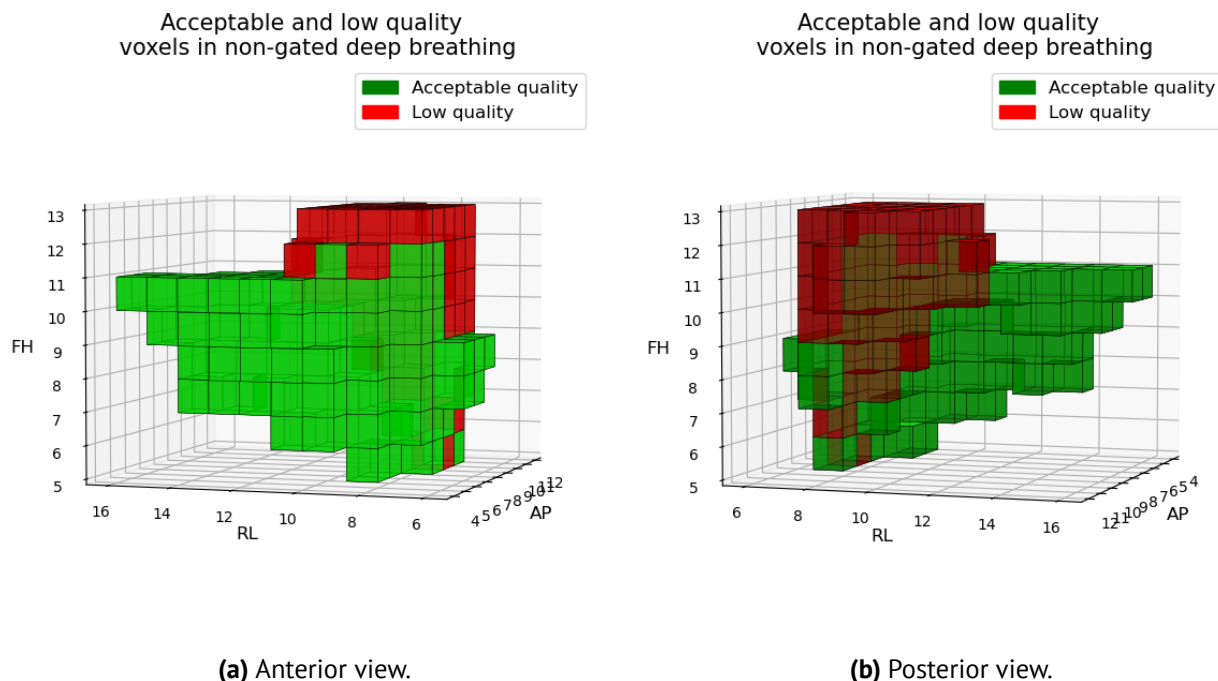
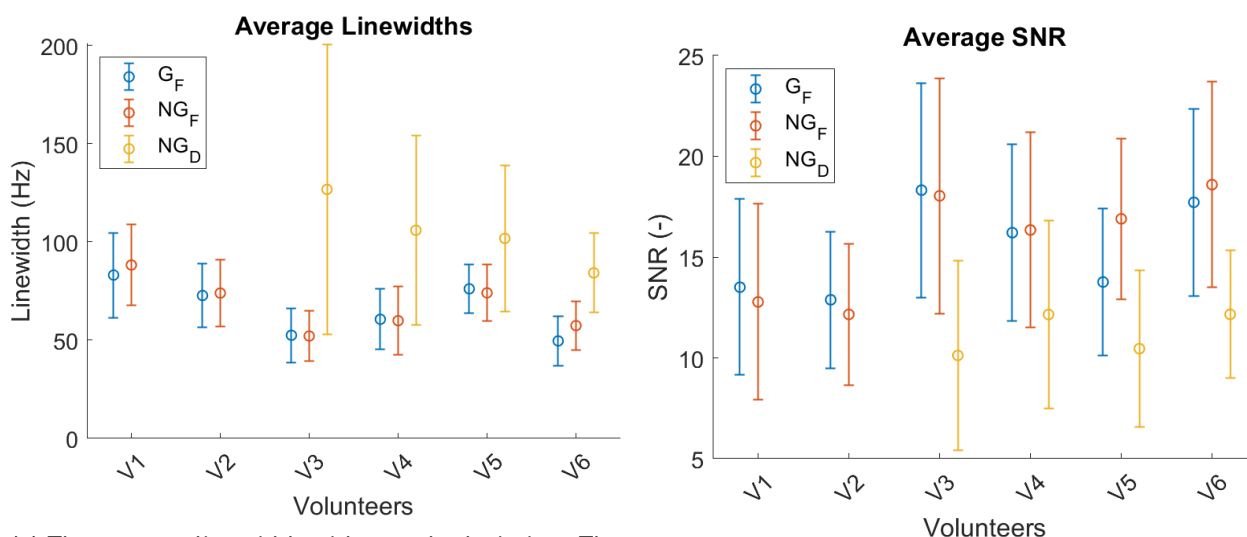


**Figure 11:** 3D visualizations of the voxels of which the overall spectrum was judged as low and acceptable quality. It was opted to do a 3D visualization, as this gives a more intuitive feeling about the spatial location of low quality voxels than a collection of maps. It can be seen that the low quality voxels are all located posterior and in the direction of the head, mainly in the 4 coronal slices near the head.

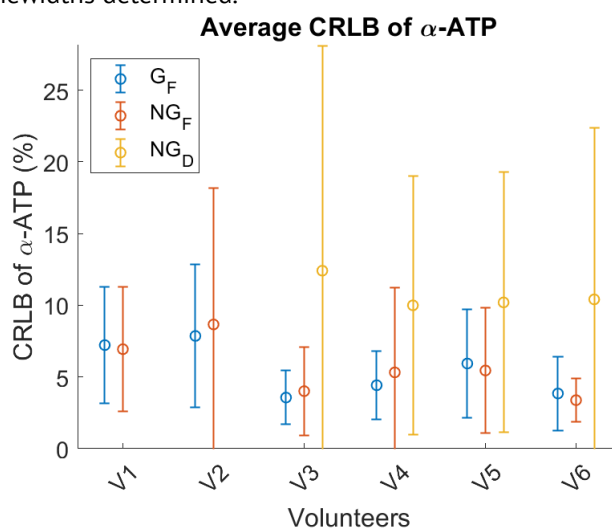
### 3.4 Objective 3: Investigate whether there is a difference in spectral linewidth, SNR and CRLB between gated acquisition with regular breathing, non-gated acquisition with regular breathing and non-gated acquisition with deep breathing in in vivo 7T $^{31}\text{P}$ -MRSI

The average linewidth, SNR and CRLB of  $\alpha$ -ATP are not clearly affected by (non)-gating in the free breathing datasets. They do seem to be affected by deep breathing, see Fig. 12.



(a) The average linewidth with sample deviation. The average linewidth is very similar for the gated and non-gated free breathing dataset, as the difference in average is much smaller than their standard deviations. The averages are not consistently higher or lower across volunteers. The standard deviations are also very similar. For non-gated deep breathing, the average linewidth is much larger. Moreover, the standard deviation is much larger, indicating that there is a wider distribution of linewidths determined.

(b) The average SNR with sample deviation. The average SNR is quite similar for the gated and non-gated free breathing dataset, as the difference in averages is much smaller than their standard deviations. The averages are not consistently higher or lower across volunteers. The standard deviations are also very similar. For non-gated deep breathing, the average SNR is much lower. The standard deviation is similar in size to those of the free breathing datasets.



(c) The average relative CRLB of  $\alpha$ -ATP with sample deviation. CRLB's over 100% are dismissed in the calculation of means and standard deviations. Number of dismissed values:  $G_F$ ,  $0.3 \pm 0.8$  values;  $NG_F$ ,  $0 \pm 0$ ;  $NG_D$ ,  $9.3 \pm 9.2$ . The average CRLB is similar for the gated and non-gated free breathing dataset, as the difference in averages is much smaller than their standard deviations. The averages are not consistently higher or lower across volunteers. The standard deviations are also similar and not consistently larger or smaller in one of the free breathing datasets. For non-gated deep breathing, compared to free breathing, the average CRLB is larger in all volunteers.

**Figure 12:** The average and standard deviation of the 6 scanned volunteers. Legend:  $G_F$  - gated, free breathing;  $NG_F$  - non-gated, free breathing;  $NG_D$  - non-gated, deep breathing.

The histograms for linewidth (Fig. 13), SNR (Fig. 14) and CRLB (Fig. 15) show that there are both individual increases and decreases observed for these properties. The effects of the individual increases and decreases dampen each other, leading to averages close to zero for the differences between free breathing datasets.

For linewidth, SNR and CRLB, the histograms of voxelwise differences between free breathing and deep breathing sets show that the linewidth, SNR and CRLB respectively increase, decrease and decrease in almost all voxels in the deep breathing scan.

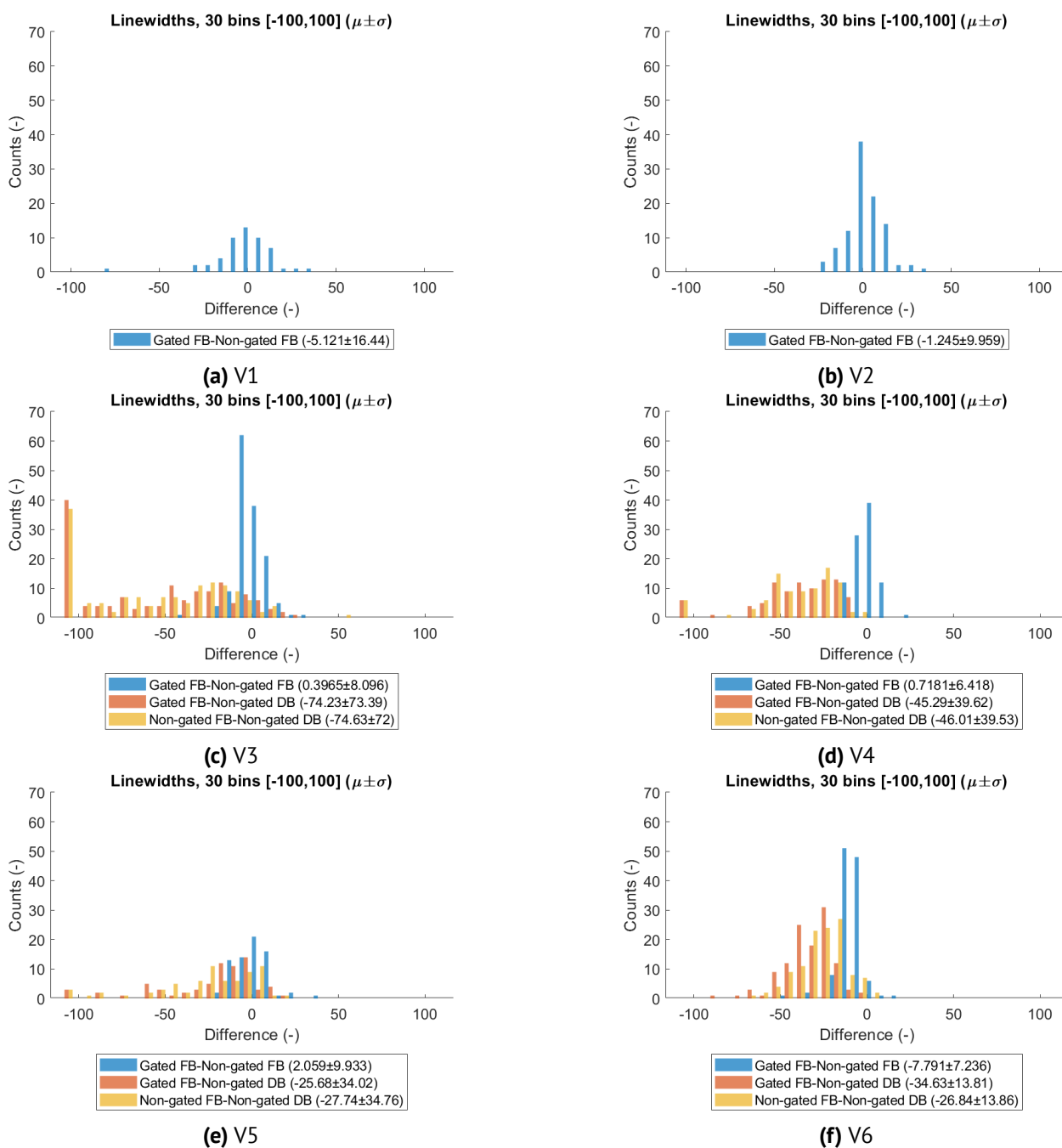


**Figure 13:** The distributions of the voxelwise differences in linewidth for all volunteers. Values that are outside of the interval  $[-100, 100]$  are binned in the bins on the outer edges. The different heights of the distribution can be explained by the different amount of voxels in the volunteers, as they all had different liver sizes. It can be seen that the average difference between gated and non-gated free breathing is not consistently positive or negative across the volunteers. Moreover, the difference distributions for both *gated free breathing - non-gated deep breathing* and for *non-gated free breathing - non-gated deep breathing* have a similar shape in each volunteer, indicating that the differences between free breathing and deep breathing are much larger than differences between gated and non-gated free breathing. It can also be seen that the difference distributions for *free breathing - deep breathing* contain mostly negative values. This indicates that for a voxel in a deep breathing scan, generally, a higher linewidth is fitted than for the same voxel in a free breathing scan.

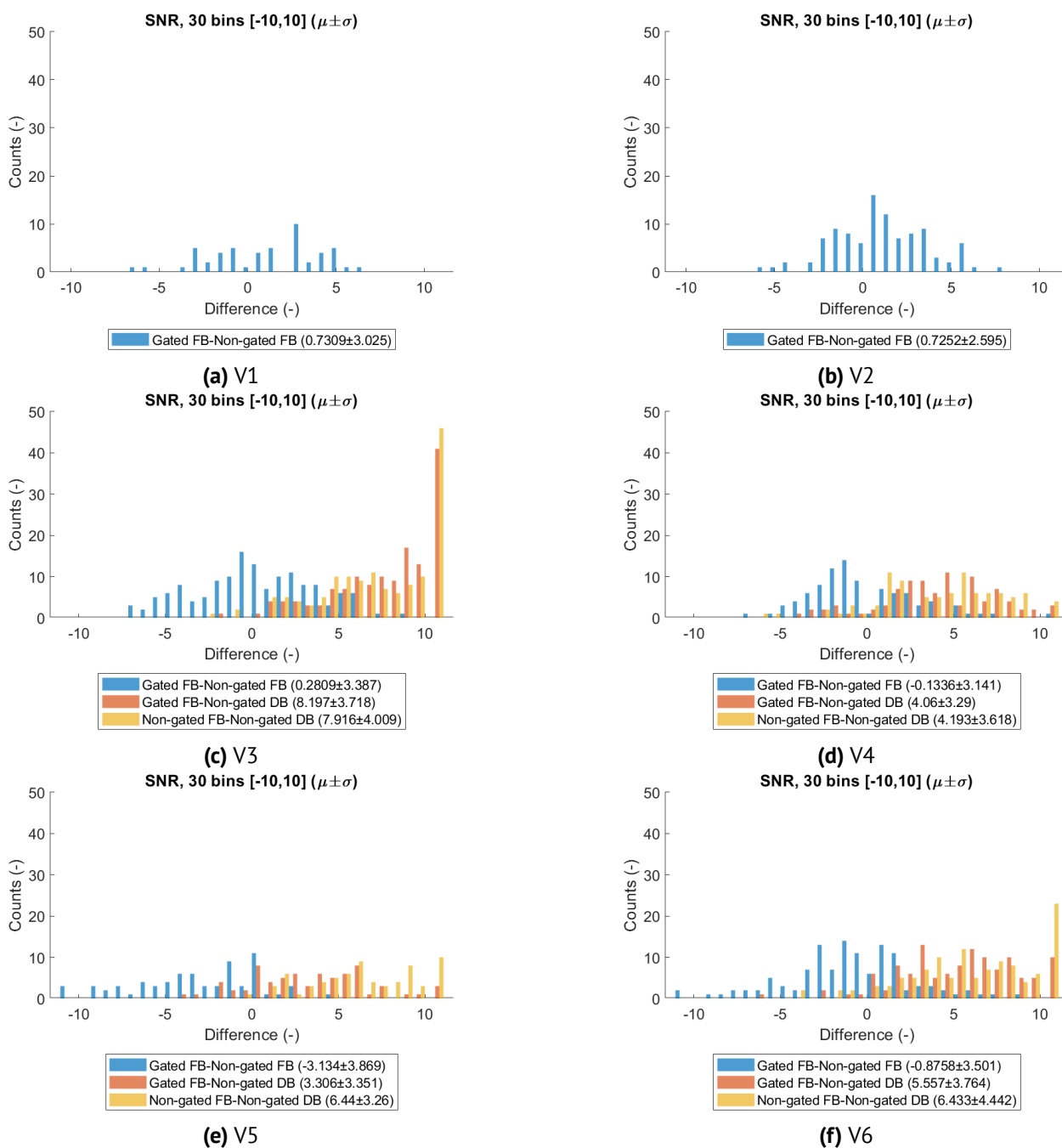


**Figure 14:** The distributions of the voxelwise differences in SNR for all volunteers. Values that are outside of the interval  $[-10, 10]$  are binned in the bins on the outer edges. The different heights of the distribution can be explained by the different amount of voxels in the volunteers, as they all had different liver sizes. It can be seen that the average difference between gated and non-gated free breathing is not consistently positive or negative across the volunteers. V5 is an outlier in these comparisons, with overall lower SNR for the non-gated free breathing dataset than for the gated free breathing dataset. The shape of the difference distributions for both *gated free breathing - non-gated deep breathing* and for *non-gated free breathing - non-gated deep breathing* have a similar shape in each volunteer, indicating that the differences between free breathing and deep breathing are much larger than differences between gated and non-gated free breathing. It can also be seen that the difference distributions for *free breathing - deep breathing* contain mostly negative values. This indicates that for a voxel in a deep breathing DB, generally, a lower SNR is determined than for the same voxel in a free breathing scan.

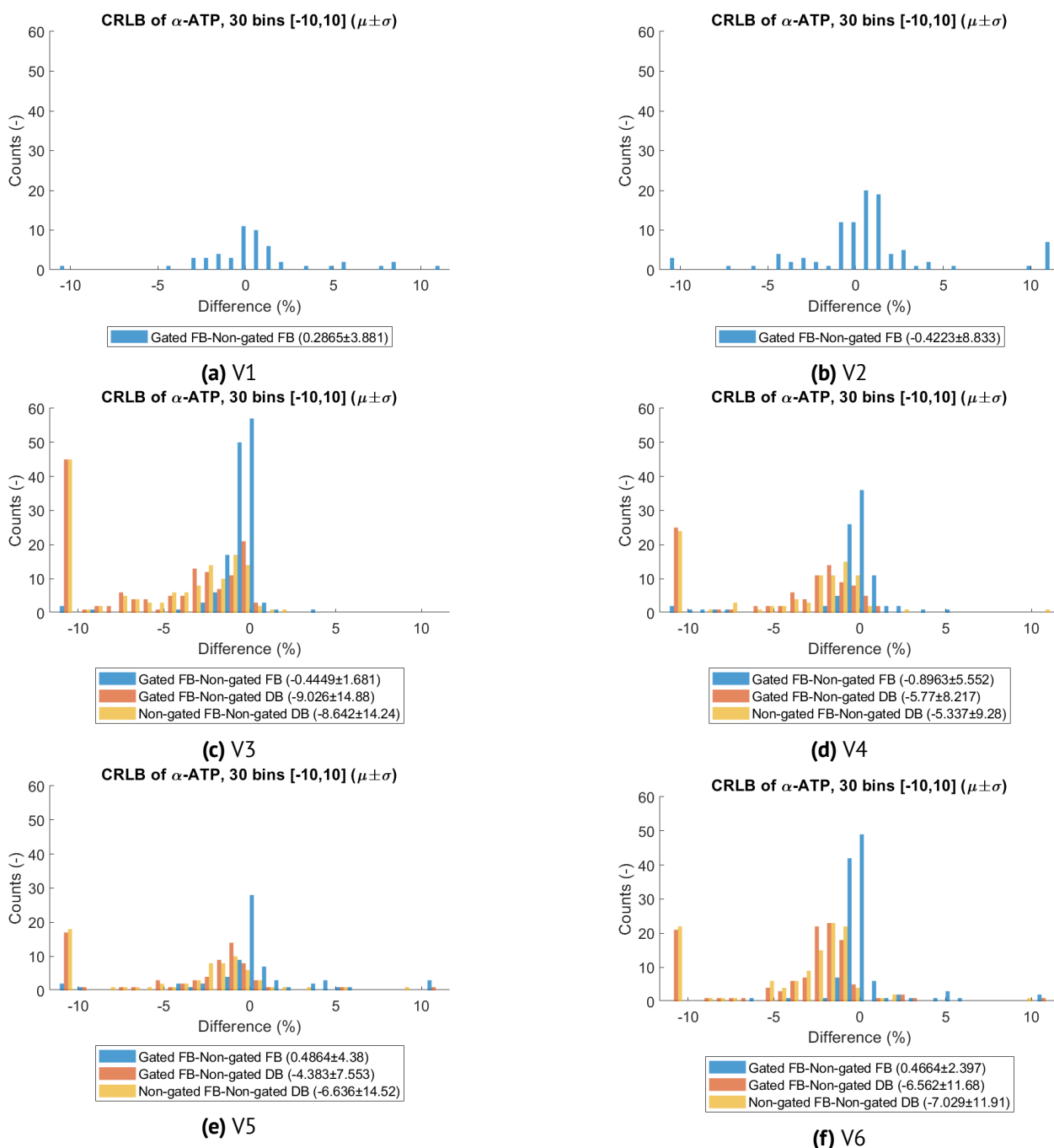


**Figure 15:** The distributions of the voxelwise differences in CRLB of  $\alpha$ -ATP for all volunteers. Values that are outside of the interval [-10,10] are binned in the bins on the outer edges. The different heights of the distribution can be explained by the different amount of voxels in the volunteers, as they all had different liver sizes. In the calculations of mean and standard deviations, CRLB's over 100% have been dismissed, see Section 2.2.6. Number of dismissed values:  $G_F - NG_F$ ,  $0.3 \pm 0.8$  values;  $G_F - NG_D$ ,  $9.3 \pm 9.2$ ;  $NG_F - NG_D$ ,  $9 \pm 9.3$ . It can be seen that the average difference between gated and non-gated free breathing is not consistently positive or negative across the volunteers. Moreover, the difference distributions for both *gated free breathing - non-gated deep breathing* and for *non-gated free breathing - non-gated deep breathing* have a similar shape in each volunteer, indicating that the differences between free breathing and deep breathing are much larger than differences between gated and non-gated free breathing. The average difference is much larger for the *free breathing - deep breathing* comparisons than for *(non)-gated free breathing* comparisons. The *free breathing - deep breathing* distributions contain mostly negative values, indicating that for a voxel in a deep breathing scan, generally, a higher CRLB is fitted than for the same voxel in a free breathing scan.

### 3.5 Objective 4: Investigate whether there is an impact on the repeatability of the quantification of concentrations of homogeneously distributed liver metabolites between gated acquisition with regular breathing, non-gated acquisition with regular breathing and non-gated acquisition with deep breathing in in vivo 7T $^{31}P$ -MRSI

From Table 10, it can be seen that between the gated and non-gated free breathing datasets, the relative CR is lower than the literature value for 12 of the 15 determined metabolites. This means that differences observed across volunteers were at least as consistent for these metabolites than in literature. Therefore, it suggests that the repeatability of a gated and non-gated free breathing scan is at least as good as that of two non-gated free breathing scans as performed in literature.

From Table 11, it can be seen that between the gated and non-gated free breathing datasets, the bias is both lower and higher than the reference values for about half of the metabolites. For comparisons between a free breathing and deep breathing dataset, all metabolites have larger biases than the reference values. This suggests that the average value is changed less by the variable gating/non-gating than by free/deep breathing.

The biases are not consistently positive across all metabolites in any of the combinations of datasets. The CR, indicating a confidence interval of  $1.96 \cdot \text{std}$ , is larger than the bias in virtually all cases, indicating that the biases are not significantly non-zero.

**Table 10:** Coefficients of repeatability (CR) for several combinations of datasets, both absolute and relative to the average value in the respective combination of datasets. Values are marked green if they are lower (<) than the literature value, blue if they are equal (=) red if they are larger (>). It can be seen that the coefficients of repeatability are lower than the literature values much more often for the combination with free breathing datasets than for combinations with the deep breathing dataset, both when expressed absolutely and relatively.

Coefficient of repeatability (CR)								
	$G_F - NG_F$		$G_F - NG_D$		$NG_F - NG_D$		Literature ( $NG_F - NG_F$ ) [39]	
	-	(%)	-	(%)	-	(%)	-	(%)
$\beta$ -ATP	1.0	8.5	1.0	8.6	1.8	16.4	1.9	13.0
$\alpha$ -ATP	0.8	4.3	1.1	6.0	1.1	5.8	0.8	3.4
$\gamma$ -ATP	1.0	5.3	1.6	8.6	1.5	8.0	0.8	3.4
Pi	0.6	7.0	1.6	18.2	1.8	20.8	1.2	13.8
GPC	0.5	7.1	3.6	56.0	4.0	61.8	0.7	16.1
GPE	0.7	9.7	2.3	32.3	1.6	22.9	1.1	25.4
PC	0.4	9.6	0.7	16.5	0.8	21.3	0.7	25.3
PE	0.3	6.3	1.6	40.1	1.4	35.3	0.7	15.0
NADH	0.6	10.0	2.0	29.0	2.1	31.0	1.8	25.1
UDPG	0.5	13.8	1.2	27.9	1.6	37.5	0.6	34.8
PtdC	0.8	40.7	1.4	70.9	0.8	43.3	0.5	30.2
PCr	1.9	22.9	3.8	44.5	3.0	34.1	0.9	24.9
PME (PC+PE)	0.5	6.1	1.6	20.2	1.5	18.9	1.0	13.8
PDE (GPC+GPE)	1.0	7.2	2.5	18.5	3.3	24.0	1.7	18.8
PME/PDE	0.1	17.3	0.1	22.4	0.1	11.7	0.2	22.7
Value $\leq$ literature	12/15	12/15	3/15	5/15	2/15	3/15		

**Table 11:** Biases of several combinations of datasets. (Relative) biases with an absolute value smaller (<) than the reference are marked green, biases with the same absolute value (=) are marked blue, biases with an absolute value larger (>) than the reference are marked red. Relative biases are calculated as a percentage of the average fitted concentration. It can be seen that about half of the biases are smaller and half are larger than the reference for the combinations of the free breathing datasets. This means that on average, the difference in average fitted concentration is similar to values in literature. For comparisons with a deep breathing dataset, biases are generally much larger. This means that the difference in the average fitted values between the deep breathing dataset and free breathing sets is larger than between the gated and non-gated free breathing dataset. Biases are not generally signed positive or negative across metabolites in any of the combinations, due to the normalization of metabolite concentrations to a total of 100% (see Section 4.2.2.2). The sum of all absolute biases of all fitted metabolites, excluding PME, PDE and PME/PDE is 0 for every comparison. Abbreviations:  $G_F$ , gated free breathing;  $NG_F$ , non-gated free breathing;  $NG_D$ , non-gated deep breathing.

	Bias						Literature ( $NG_F - NG_F$ ) [39]	
	$G_F - NG_F$		$G_F - NG_D$		$NG_F - NG_D$		(-)	%
	(-)	%	(-)	%	(-)	%		
$\beta$ -ATP	-0.07	-0.6	0.41	3.7	0.57	5.1	-0.23	-1.5
$\alpha$ -ATP	0.16	0.8	1.73	9.5	1.67	9.2	0.07	0.3
$\gamma$ -ATP	-0.06	-0.3	-0.30	-1.6	-0.25	-1.3	0.08	0.3
Pi	0.05	0.5	0.64	7.3	0.46	5.3	-0.07	-0.8
GPC	0.21	3.0	1.09	16.8	0.92	14.3	0.03	0.6
GPE	-0.40	-5.6	0.06	0.9	0.38	5.4	0.01	0.1
PC	-0.04	-1.1	-0.32	-8.1	-0.28	-7.1	0.08	2.9
PE	0.17	4.0	0.77	18.7	0.53	13.4	-0.07	-1.6
NADH	0.12	1.9	-0.90	-13.4	-1.09	-16.4	-0.18	-2.9
UDPG	0.06	1.6	-0.80	-18.7	-0.92	-21.7	-0.02	-1.1
PtdC	0.06	2.7	-0.17	-8.6	-0.32	-16.7	0.11	6.7
PCr	-0.25	-3.1	-2.20	-26.1	-1.69	-19.4	0.19	5.4
PME (PC+PE)	0.13	1.6	0.45	5.5	0.25	3.2	0.01	0.1
PDE (GPC+GPE)	-0.19	-1.3	1.15	8.5	1.30	9.6	0.03	0.4
PME/PDE	-0.01	-1.0	-0.08	-12.1	-0.09	-13.4	0.02	-1.8
Value $\leq$ literature	7/15	8/15	0/15	0/15	0/15	0/15		

### 3.6 Objective 5: Investigate whether the effects of ghosting can be reduced effectively with a REST slab suppressive sequence on a phantom simulation of respiratory motion of the stomach with 1.5T $^1H$ -MRSI

#### 3.6.1 Feasibility of REST slab suppression

In Fig. 16, it can be seen that it is possible to position a REST slab suppressive sequence in a way that the regions containing the portal vein and stomach are completely separated.

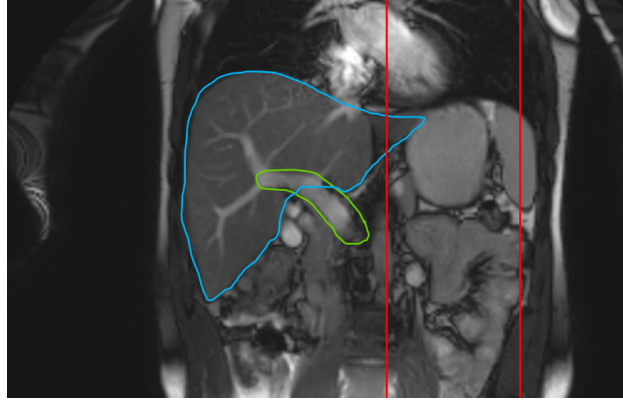


**Figure 16:** Green: outline of portal vein. Blue: outline of liver. Red: outline of an area which could be selectively suppressive with a perfect REST slab.

The slice is positioned so that the stomach does not leave the desired region during respiratory motion. Based on visual judgment, the sequence can be positioned so that the portal vein is unaffected, in the case of perfect selectivity. The liver cannot be completely separated from the stomach using an ideal rest slab suppressive sequence, but the largest part of the liver can be spared.

### 3.6.2 Phantom experiment with acetone container, scanned with $^1H$ -MRSI at 1.5T

For the design of the phantom experiment, the results of Experiment 1 (in vivo 1.5T MRI) are used. The acetone container is moved with 3.5 cm, representing deep respiratory motion.

In Fig. 17, it can be seen that in the voxels with the lowest signal intensity, there is still a clear signal noticeable in the noise. Moreover, multiple peaks are visible in the *no-motion* scan, while no peaks were expected. This is discussed further in Section 4.2.3.

## Ghosting in low signal voxel

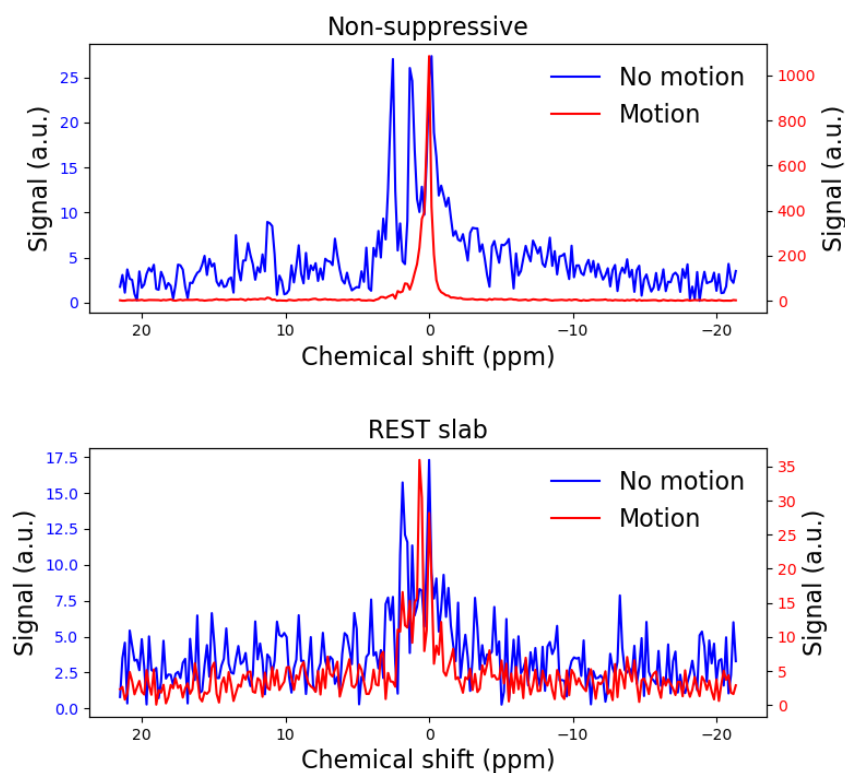


**Figure 17:** The signal in the voxels with the lowest signal intensity in the *no-motion* scan in the non-suppressive and the REST slab suppressive scans. Note the independent y-axes. The x-axis is calibrated with the transmit frequency at 0 ppm. It can be seen that in the voxel with the lowest signal, the signal is still larger than the noise for both acquisitions. Moreover, it can be seen that the signal increases about 40 times in the non-suppressive scan with the moving container, and only about 2 times in the rest-slab scans.

In Fig. 18, it can be seen that the maximum signal intensities are lower for the REST slab scan than for the non-suppressive scan, as expected. The REST slab reduces the signal of the acetone container. In this scaling, no ghosting effects can be observed.

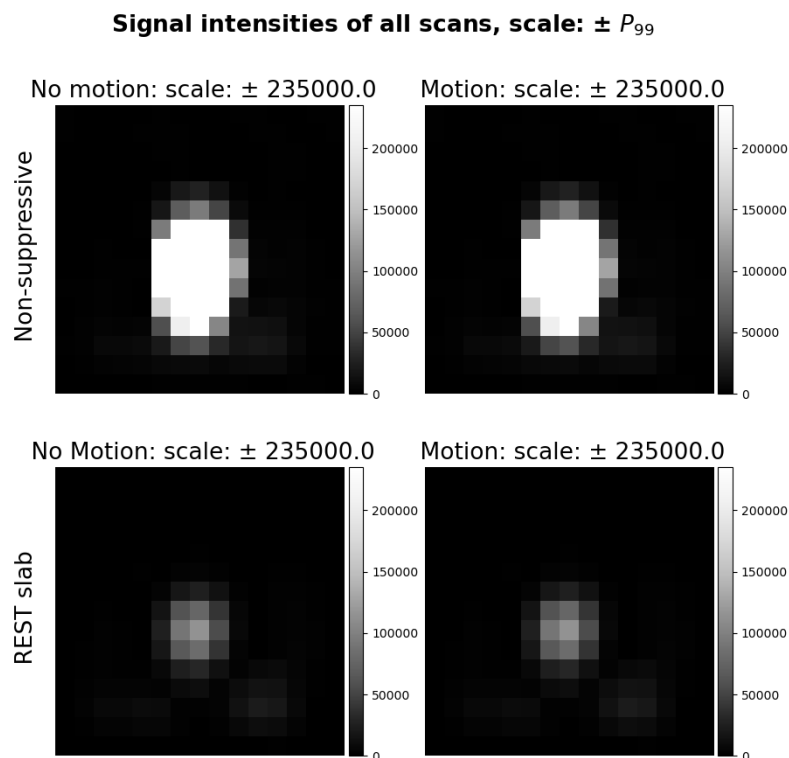
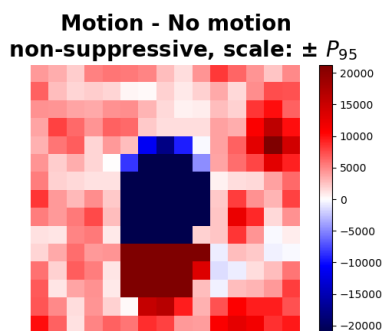
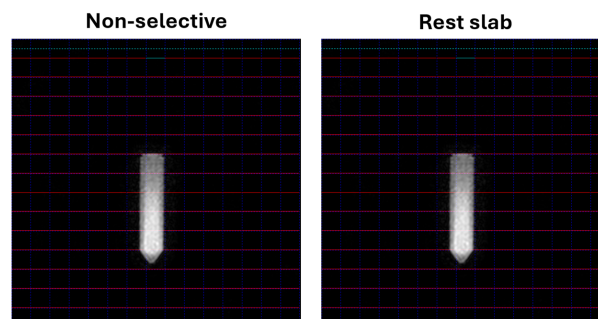


**Figure 18:** The signal intensities of the same slice of every performed scan. The display limits are set to be  $\pm (99^{\text{th}} \text{ percentile of absolute values})$ , taken over all 4 datasets together. It can be seen that the maximum signal intensities are much lower in the REST slab scan than in the non-suppressive scan. However, subtle differences cannot be seen in this scaling. Fig. 19a shows the difference in intensities between the datasets in the top row. Fig. 20 shows the difference in intensities between the top row and the bottom row. The reference position of the container can be seen in Fig. 19b. Movement is from top to bottom. Units are arbitrary.

In Fig. 19 it can be seen that the signal increases a lot in the non-suppressive scan in the voxels that do not contain the acetone container in the *motion* scan *no motion* scan. This signal increase is expected to be the ghosting effect.



(a) The change in signal intensity is shown in red for a higher signal in the *no-motion* dataset and blue for a higher signal in a *motion* dataset. The display limits are set to be  $\pm$  (95<sup>th</sup> percentile of absolute differences), so that the 95% smallest differences are displayed on a continuous color map. Units are arbitrary. A slice through the acetone container is chosen, parallel to the table. Motion is from top to bottom, in FH direction (for a patient lying head first in the scanner). It can be seen that the signal is higher in the *no-motion* scan in all voxels that are not in the center of the slice. At the location of the acetone container in the *no-motion* scan, the signal is lower in the *motion* scan. In the path of the acetone container, the signal is higher in the *motion* scan.



(b) The image matching the difference overview of Fig. 18 and 19a. Motion is from top to bottom, in FH direction.

**Figure 19:** The difference in signal intensity between two regular  $^1H$ -MRSI scans with a moving and a stationary acetone container.

In Fig. 20, it can be seen that the signal in the acetone container is lower in the REST slab suppressive scan than in the non-suppressive scan in both the *no-motion* and *motion* scans. In the voxels that do not contain the acetone container, the signal increases more in the non-suppressive scan than in the REST slab suppressive scan.

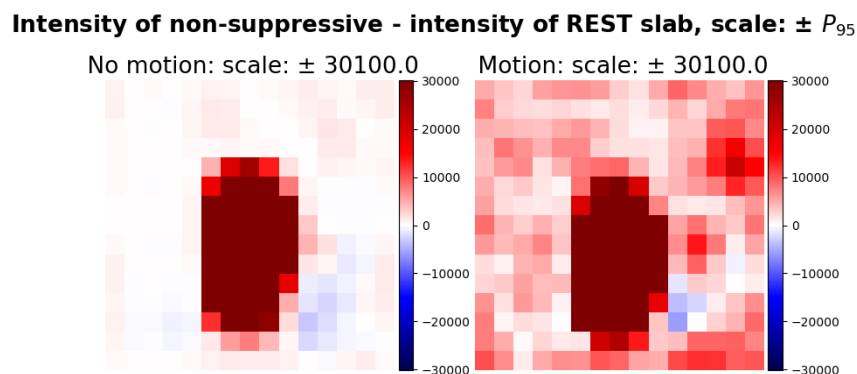


**Figure 20:** The difference in intensity per voxel of the non-suppressive scan and the REST slab suppressive scan. The intensity has arbitrary units. It can be seen that in both the *no-motion* and *motion* dataset, the signal at the location of the acetone container is higher in the non-suppressive scan. In the *no-motion* datasets, the signal is generally higher in the non-suppressive dataset than in the REST slab suppressive dataset. In the *motion* datasets, the signal is much higher in the non-suppressive dataset than in the REST slab suppressive dataset. Also, in some of the regions where the REST slab suppressive signal was higher than the non-suppressive signal in the *no-motion* set, the signal is now also much higher in the non-suppressive scan. It can be seen that the difference in signal intensities in the areas without the acetone container is much larger in the *no-motion* dataset than in the *motion* dataset. The blue area is likely due to residual water.

In Table 12, it can be seen that the total signal in noise-like voxels increases in the *motion* scan much more in the non-suppressive scan than in the REST slab suppressive scan. The reduction in signal in the acetone container itself in the REST slab suppressive scan compared to the non-suppressive scan (see Table 13) is in the same order of magnitude as the reduction in observed ghosting.

**Table 12:** The ratio of  $\frac{motion}{no-motion}$  of the sum of the signal in the 10% voxels with the lowest *no-motion* signal. The signal increase in the scan with the moving acetone container is much greater in the non-suppressive scan compared to the REST slab suppressive scan, indicating that the REST slab suppressive scan experiences less ghosting, as expected.

Ratio of total signal ( <i>motion</i> / <i>no-motion</i> )	
Non-suppressive	17.9
REST slab suppressive	1.2

**Table 13:** The maximum signal intensity in the *no-motion* scans of both the non-suppressive and REST slab suppressive scan. The same voxel in the acetone container is chosen in the non-suppressive and REST slab suppressive scan, which has the maximum signal intensity in the *no-motion* scan in both datasets. The units are arbitrary. It can be seen that the maximum signal intensity is 20.5 times lower in the REST slab suppressive scan than in the non-suppressive scan.

	Maximum signal intensity (-)
Non-suppressive	237e4
REST slab suppressive	11.4e4
Ratio (non-suppressive/REST slab suppressive)	20.5

## 4 Discussion

The structure of this section is as follows: First, the results are interpreted and related to the objectives stated in the introduction. Second, The experimental shortcomings and improvements are discussed per experiment. Recommendations will be made that can improve the experiments. Third, a general discussion is written that reflects on the thesis in general, places it in a larger context and does suggestions for interesting further research directions and improvements on the experiments that are not directly related to shortcomings of the current experiments.

### 4.1 Discussion of results

#### 4.1.1 Objective 1: Investigate the amount of motion of the liver, portal vein, stomach, diaphragm and gall bladder in regular and deep breathing by MRI

##### 4.1.1.1 Respiratory motion

In Experiment 1 (in vivo 1.5T MRI), it was found that the tracked structures have very similar respiratory motion in free breathing. As a result, the assumption that the liver and portal vein are subject to similar respiratory motion holds.

This assumption was needed to justify the choice of In vivo  $^{31}\text{P}$ -MRSI measurements as a substitute for portal vein  $^2\text{H}$ -MRSI. Moreover, based on these results, it was decided that the acetone container in the phantom experiment should move 3.5 cm to simulate deep breathing.

The proximal part of the portal vein moved less than the distal part in deep breathing. Therefore, it may be recommended to look at the portal vein in the proximal part if a patient has a large respiratory amplitude.

In Experiment 2 (in vivo 7T MRI &  $^{31}\text{P}$ -MRSI), the movement of the diaphragm was determined as this information could be useful in explaining findings in the  $^{31}\text{P}$ -MRSI results. In these measurements, a generally larger amplitude of both deep and regular respiratory motion was found than in Experiment 1, although there were also volunteers with breathing motion in the same order of magnitude. This could be due to several reasons.

It could be (partially) due to natural variation in respiratory motion. Possibly, the sample size in experiment 1 was too small for a realistic estimation of respiratory motion.

The different amplitudes for deep respiratory motion could be due to differences in breathing instructions. In Experiment 1 (in vivo 1.5T MRI), the volunteers were simply instructed to breathe deeply, whereas in Experiment 2 (in vivo 7T MRI &  $^{31}\text{P}$ -MRSI), the volunteers were instructed to follow a breathing pattern. This breathing pattern may have led to deeper respiratory motion.

The found respiratory motion amplitudes were within the order of magnitude of literature values.

##### 4.1.1.2 Morphology

The size and variance of the portal vein is within the range expected from literature. As a result, there is no reason to assume that there are errors caused by incorrect voxel size or mistakes in processing in the distances reported in our motion measurements. Moreover, the gall bladder is within the expected size range and roughly similar in size to the portal vein. However, there is a large variety in shape and rotation of the organ. As the gall bladder is subject to similar motion and has a more similar size to the portal vein than the liver, it could be an interesting research direction to investigate motion effects on the gall bladder instead of the liver using  $^{31}\text{P}$ -MRSI. For more explanation, please see Section 4.3.4.1

#### 4.1.2 Objective 2: Investigate whether quality of spectra differs between gated acquisition with regular breathing, non-gated acquisition with regular breathing and non-gated acquisition with deep breathing in in vivo $7T$ $^{31}P$ -MRSI

Very few spectra were judged as low quality in the free breathing acquisitions. In the deep breathing acquisitions, a very large part of the spectra was judged as low quality.

As the same amount of spectra are subjectively judged as acceptable quality in both free breathing scans, and the low quality spectra are all explainable by the fact that they are at the border of the liver, this study does not suggest that the quality of spectra decreases by not performing gated acquisition on the liver. However, the manual judgments should definitely be repeated for more volunteers and a larger range of respiratory motions.

It should be studied if the observation that there is no difference in spectral quality between gated and non-gated free breathing scans also applies to the portal vein. The few voxels that were of low quality in the liver were all located at the border of the tissue. As the portal vein is much smaller, the majority of voxels will be located at the border of the tissue. Therefore, the spectral quality of the portal vein may be more sensitive to respiratory motion and respiratory gating.

As many spectra are judged as low quality in the deep breathing scan, this study suggests that deep breathing affects the quality of spectra in the liver. The low quality spectra were not scattered throughout the volume in the deep breathing scan, but were mostly located near the top of the volume in 4 slices. This is a distance of 8 cm, which is also the respiratory motion amplitude of this volunteer. This may indicate that movement of the lungs was the primary cause of spectral worsening. This relationship should be investigated in more volunteers. In patients with deep respiratory motion, it is recommended to perform gating or, if possible, instruct the patient to breath shallowly.

During the visual judgment, the fitted metabolite concentrations were also inspected. This criterion has not been used in the thesis in the end. Some errors that were found quite often in the metabolite concentrations, especially when there is a strong suspicion that the spectrum has had an incorrect frequency shift, was a misclassification of GPC as GPE and of PE as PC. Generally, these concentrations are roughly in the same order of magnitude in well-defined spectra. However, quite often, one metabolite would strongly increase in fitted concentration whilst the other metabolite would be much smaller.

#### 4.1.3 Objective 3: Investigate whether there is a difference in spectral linewidth, SNR and CRLB between gated acquisition with regular breathing, non-gated acquisition with regular breathing and non-gated acquisition with deep breathing in in vivo $7T$ $^{31}P$ -MRSI

The linewidth, SNR and CRLB all show a similar result, where they are not clearly different in gated and non-gated free breathing scans and clearly worsen in non-gated deep breathing scan.

##### 4.1.3.1 Linewidth

The average linewidth was very similar for the gated and non-gated free breathing datasets. The differences were generally well within the standard deviation. Therefore, not performing respiratory gating is not expected to lead to an increase in linewidth in subjects with regular respiratory motion.

The average linewidth increased a lot in subjects with deep respiratory motion. Moreover, the standard deviation increased a lot. This may be in part due to spectra that are of very low quality and in which large linewidths are used to fit them as good as possible. It was observed in volunteer V3 that the linewidth increased in virtually every voxel. As less than half of the spectra were judged as low quality, it is expected that the linewidth also increases in spectra of relatively acceptable quality in the deep breathing dataset.

The standard deviation in the non-gated deep breathing set seems correlated to the amplitude of the deep respiratory motion. It would be interesting to see whether in these volunteers, the linewidth is really caused by deep respiratory motion. To investigate this, the quality of the spectra of these 4

volunteers should be inspected and the relationship between linewidth and respiratory motion should be explored in the spectra of acceptable quality.

Based on a preliminary study [22], it was expected that non-gated free breathing would lead to a worsening of spectra and increase in linewidth. An explanation for the fact that it was observed in that study, but not in this thesis is that the subject of [22] breathed deeply during the first phase of the measurement. That is the moment that low spatial frequencies are recorded in the sequence, which contribute the most to the general shape of the signal. This may have seriously affected the spectra.

#### 4.1.3.2 SNR

The average SNR was very similar for the gated and non-gated free breathing datasets. The differences were generally well within the standard deviation, which is also similar for both free breathing datasets. Therefore, not performing respiratory gating is not expected to lead to a decrease in SNR in subjects with regular respiratory motion.

The average SNR is a lot lower for the deep breathing dataset than for the free breathing datasets. Moreover, the SNR decreases in almost every voxel. This indicates that deep respiratory motion does have a large effect on the SNR, and that the lower SNR is not only due to the presence of low quality spectra. The standard deviation is similar in size as the free breathing datasets. This may be due to the fact that SNR does not increase as a result of respiratory motion, and therefore the range of values that SNR can have is limited between 0 and the SNR of a good spectrum. The linewidth, however, can become much larger in bad spectra, leading to a larger standard deviation.

#### 4.1.3.3 CRLB

The average CRLB was very similar for the two free breathing datasets. The standard deviation was less similar, but did not differ in a consistent way. The average CRLB of the free breathing sets was always well within each others standard deviation. Based on CRLB, there does not seem to be a large difference in quality of spectra between the gated and non-gated free breathing scan.

The average CRLB and its standard deviation are much larger for the deep breathing dataset. This indicates that the quality of spectra may be much worse than the free breathing datasets.

#### 4.1.4 Objective 4: Investigate whether there is an impact on the repeatability of the quantification of concentrations of homogeneously distributed liver metabolites between gated acquisition with regular breathing, non-gated acquisition with regular breathing and non-gated acquisition with deep breathing in in vivo $7T$ $^{31}P$ -MRSI

The effect of (non) gated acquisition on the quantification error is investigated by investigating whether the (non) gated scans could be identical. This is done by determining the coefficient of repeatability (CR) and bias.

It was found that the CR of the combination of gated and non-gated free breathing scans were in most cases smaller than literature values for 2 non-gated free breathing scans. Moreover, biases were similar in size compared to literature. Therefore, no evidence was found that not performing respiratory gating leads to an increase in variability in quantified concentrations that is larger than the naturally expected variation.

It was also found that the CR for combinations of free breathing with deep breathing datasets was larger than the naturally expected CR for almost all metabolites. Moreover, the bias was larger than the naturally expected bias for all metabolites. This suggests that deep respiratory motion leads to a large increase in variability in quantified concentrations, much larger than the naturally expected variation.

Given that about half of the deep breathing spectra was judged as low quality, the fitted deep breathing values have a bias that may be surprisingly small. This is because in every spectrum, the summed total of concentration is always normalized to 100%. Therefore, the possible influence on quantified

concentrations is automatically limited to values between 0 and 100. For a further discussion of this method of normalization, please see Section 4.2.2.2.

#### 4.1.4.1 Difference in SNR

In Appendix A.1, it can be seen that the SNR of the measurements performed are lower than the SNR of the measurements that are used for the repeatability comparison. Spectra with lower signal are expected to be subject to larger variations in fitted concentrations [38]. Therefore, the conclusion that the repeatability of the performed measurements is at least as good as the reference measurements is only strengthened by the lower SNR.

#### 4.1.5 Objective 5: Investigate whether the effects of ghosting can be reduced effectively with a REST slab suppressive sequence on a phantom simulation of respiratory motion of the stomach with 1.5T $^1H$ -MRSI

The decrease in signal in the non-suppressive scan in the *no-motion* location of the acetone container in the *motion* scan compared to the *no-motion* scan, makes intuitive sense as the container spends less time in those voxels if it is moving. This also explains the increase in signal in the path of the acetone container.

In the non-suppressive scan, it was very clear that the moving container led to an increase in signal in voxels with low signal. This experiment therefore supports the hypothesis that ghosting is present in the in vivo measurements. The difference is so large, that it is expected to be significant and not due to any of the several experimental challenges. Therefore, the phantom was sufficiently adequate to simulate the ghosting effect due to respiratory motion of the stomach.

The REST slab suppressive sequence was very effective in reducing ghosting. The signal increases much more as a result of movement in the non-suppressive scan than in the REST slab suppressive scan, in voxels that do not contain the acetone container.

The REST slab suppression reduced the acetone signal a lot, but not completely. This may be in part due to some recovery of magnetization between the suppression pulse and the excitation pulse.

## 4.2 Experimental discussion

### 4.2.1 Experiment 1: In vivo MRI scans at 1.5T for respiratory motion, organ size and visualization

In the in vivo MRI scans for measuring respiratory motion and organ size and for visualization of the placement of the REST slab, there were a few experimental aspects that could be improved and circumstances that should be taken into account.

#### 4.2.1.1 Variation in respiratory motion

There were large differences observed in respiratory motion between volunteers. Moreover, the respiratory motion was generally smaller than in Experiment 2 (in vivo 7T  $^{31P}$ -MRSI in the liver and MRI). This dissimilarity should be resolved to find a representative motion amplitude in the phantom measurements (Experiment 3).

It is recommended to increase the population size to see if this resolves the dissimilarities and to simulate more accurate respiratory motion in phantom experiments. Moreover, it is recommended to investigate if there is a difference in deep breathing amplitude between simply asking the volunteer to breathe deeply and letting them follow the box breathing pattern.

#### 4.2.1.2 Variation in organ morphology

The sizes of the portal vein measured were relatively large, but within the expected range. The morphology of the portal vein was different in the volunteers, as one volunteer did not have visible branching. This made it difficult to apply an identical definition of portal vein length in all volunteers.

A larger population size could allow for a larger population for every possible portal vein morphology, which allows for separate definitions of portal vein length and more accurate estimates.

The dimensions of the gall bladder were difficult to measure, because it had a different morphology in every volunteer. This can be explained by the fact that there are many anatomical variations in system of liver, gall bladder and bile ducts. The gall bladder can be cylindrical, hourglass shaped or pear shaped for example [55]. As the measurements are different in all gall bladders, the standard deviation is not reported.

To better measure organ size, it would be valuable to perform 3D scans over 2D multi-slice scans. This would allow for a full segmentation of the organ and for a calculation of the volume of the organ. This would be especially valuable for the gall bladder, which comes in various shapes and positions, leading to challenging measurements. Acquiring 3D images would allow the whole gall bladder volume to be segmented, which is a better measure for comparing organ sizes than the diameter. 3D scans would also allow for measurement of stomach volume, which can be used for a more realistic phantom in Experiment 3.

As the organ sizes were within the expected range, the aforementioned improvements are not expected to change the conclusion that portal vein and gall bladder are of similar size.

#### 4.2.1.3 Imaging of deep respiratory cycle

For deep respiratory motion, often the full respiratory cycle was not visible in the coronal scan, leading to a possible underestimation of breathing motion. This is also suggested by the values in Table 7. In free breathing, the feet-head respiratory motion of the portal vein is similar in the sagittal and coronal view, with the sagittal measurement giving a slightly lower value. In deep breathing, the measured respiratory motion is much larger in the sagittal measurement, where the portal vein was visible in every frame. It is not investigated whether the difference is significant, as the sample size is very small. If the respiratory motion is underestimated, the current phantom setup in experiment 3 may also simulate too little ghosting as the motion of the acetone container is based on this information.

It is strongly recommended to focus on accurate slice positioning for deep respiratory motion, combined with larger slice thickness. A 3D scan could be investigated, so that structures cannot move out of the scan plane.

#### 4.2.1.4 Implementation of motion measurement

The respiratory motion was estimated as the amplitude between the maximum and minimum marked location of a structure. This made it sensitive to only two marked values out of the entire marked dataset, the minimum and the maximum value. An outlier check was performed to prevent large errors by this method, but still, it was sensitive to some overestimation of the average respiratory motion. This method was applied consistently across the volunteers, so any bias should at least be similar for all volunteers. Moreover, in this study, it is better to overestimate respiratory motion than underestimate it, as it will lead to a phantom study that studies a worst-case-scenario instead of an optimistic scenario.

An improvement would be to incorporate averaging in the determination of the respiratory motion over the simple difference between the minimum and maximum value, reducing the sensitivity to outliers. Alternatively, if a structure is marked at every scanned time point in the respiratory cycle instead of only at the minimum and maximum locations, it should be possible to fit the movement as a periodic signal. This allows for accurate interpolation of the organ locations.

#### 4.2.2 Experiment 2: In vivo $^{31}\text{P}$ -MRSI scans for investigating the quality of spectra, spectral linewidth, SNR, and CRLB, and quantification of spectra

In Experiment 2, multiple methodological choices were made that are explained and discussed further here. Moreover, some shortcomings are discussed as well as suggestions to improve on these shortcomings.

#### 4.2.2.1 Statistics

In Experiment 2, statistical tests were not used and instead, qualitative descriptions of the quantitative results were used. This is done, because for statistical tests, it is important that samples are independent. However, in this experiment, each sample was a voxel and neighbouring voxels were not independent measurements, as they were directly influencing each other through the PSF. A solution for this could have been to analyze voxels with at least 2 voxels of spacing between them. This would reduce the sample size a lot, however. As the number of volunteers was also quite limited, it was decided to refrain from significance statements and present this work as a proof-of-principle study.

#### 4.2.2.2 Choice of measure for impact on quantification

The impact of (non) gating on the quantification of metabolites was focused on repeatability instead of the actual fitted concentrations for two reasons.

The first was that repeatability results could be compared with literature. In this study, no reference scan was performed, such as a second non-gated free breathing scan. Therefore, the result of any other measure that would say something about differences in quantification between two datasets, could not be corrected for inherent differences due to natural variance.

The second reason was that the magnitude of the determined concentrations are not expected to necessarily increase or decrease due to (non) gating or deep breathing because of the normalization. In every spectrum, regardless of its actual quality or height of peaks, the total amount of fitted concentrations is normalized to be 100%. Therefore, a poor quality spectrum in which only one peak can be fitted will yield a very high concentration for that peak. Moreover, in a high quality spectrum in which many metabolites can be fitted, the determined concentrations for every separate peak will be lower as the total amount of fitted concentrations is fixed.

The effects of this normalization can actually be seen in Table 11. If all the absolute biases for a given comparison are summed, excluding the biases for PME, PDE and PME/PDE, the sum will be 0 as any increase in a concentration of any metabolite must lead to a decrease in concentration of some other metabolite. Therefore, the magnitude of the determined concentration is not a good measure for the impact of respiratory motion.

In contrast, the repeatability analysis should work. Due to the normalization, concentrations are expected to fluctuate a lot in datasets with worse spectra, because it is expected that there is more variation in the quality of spectra and more variation in which peaks are fitted best. This increased variance would lead to worse repeatability results, which is indeed observed in this thesis for the deep breathing scans.

An important sidenote on the repeatability analysis is that the setup and processing was not completely identical with the reference experiment [39]. The determined SNR in this was quite a bit lower than the reference setup, see Appendix A.1. It is known that the current setup has a newer  $B_1$  coil. The new coil is stronger than the previous coil, and therefore would be expected to have a better SNR. Therefore, it is unclear what exactly causes this difference.

Therefore, it is recommended to acquire a second non-gated free-breathing scan for every volunteer, to have a direct comparison to determine any possible effects due to (not) gating or deep breathing without any possible experimental differences.

#### 4.2.2.3 Choice of normalization

A different method of expressing the concentrations is to express them as a ratio of the fitted concentration of  $\gamma$ -ATP. The benefit of this is that concentrations are not influenced by variations of other metabolites. This was also investigated in this study, but led to extremely high concentrations in multiple low quality spectra. In these spectra, no  $\gamma$ -ATP was fitted, leading to an enormous ratio.

The output of AMARES itself could also have been used without any normalization to (a sum of) other signals. It was decided not to do this for two main reasons. Firstly, the methodology would become less representative of current practice. Unscaled values would vary greatly between volunteers and

setups and therefore have little interpretative value for investigating e.g. diseases or metabolic processes. Secondly, any results found could not be compared to a literature value, as is possible with the repeatability results.

#### 4.2.2.4 Determination of SNR

SNR was determined in the spectral domain in this thesis. However, the method used is not one of the generally recommended methods of SNR determination [40]. This method was chosen to be able to compare results as good as possible to the reference article [39].

This method of SNR determination is sensitive to an incorrect frequency shift of the spectrum, as the signal intensity is defined as the maximum value in a specific interval of the spectrum. As there were some very noisy spectra in the deep breathing scans, this may have led to an incorrect frequency shift and possibly an imperfect SNR calculation. A more robust method of calculating SNR would be to do it on the time domain signal (FID). This could be done by using the first point of the FID as signal, which should be equal to the area under the entire spectrum [40]. It was investigated whether it was possible to implement this method in this study, but this was challenging in the used reconstruction pipeline.

#### 4.2.2.5 Determination of CRLB

It was chosen to use the CRLB of  $\alpha$ -ATP, as the average  $\alpha$ -ATP both had a large average value and a small standard deviation in the average.  $\gamma$ -ATP had a similarly large average value and small standard deviation, but as the SNR determination was also based on  $\alpha$ -ATP, it was decided to base both measures on the same metabolite.

#### 4.2.2.6 Visual judgment of distinctiveness of peaks

Most of the criteria were subjective. Moreover, the spectra may not have been judged exactly in the same way. The judgment process took quite a long time and during the process, the experience in recognizing patterns in the spectra increases. This may lead to a changing perception of the quality of spectra.

Improvements on this would be to define criteria for the quality of spectra that are as objective as possible, such as the noisiness of the residual after fitting, an SNR value for the peaks of interest and physiological plausibility of fitted metabolite concentrations. Another improvement could be to investigate inter- and intra-observer variability.

### 4.2.3 Experiment 3: $^1\text{H}$ -MRSI at 1.5T on a phantom simulation of respiratory motion of the stomach

Experiment 3 contained some shortcomings in the setup that strongly influenced the methods used to extract results from the data. The experiment has had multiple iterations in which it was attempted to reduce several of these shortcomings, but these experiments all had their own problems and did not provide additional useful information for the stated objective. The main shortcomings of the described setup are the residual water in the phantom and inconsistent shimming and power optimization.

#### 4.2.3.1 Phantom

The phantom contained some water droplets. The phantom had been reused from an older experiment, for which the phantom was filled with water. It was not possible to completely remove all the moisture without physically destroying parts of the phantom. The water droplets generated quite some signal, which limited the interpretability of the data.

It was not possible to assume that all signal measured inside the volume must originate from the acetone, and therefore it is challenging to simulate the relationship between distance from the signal source and ghosting effects. It would be interesting to research this relationship, as it is expected that the ghosts would decrease in magnitude further from the acetone container, if the ghosting behaves as it does in MRI [33].

If the experiment were repeated with the same setup, the phantom should be completely dry. This can be achieved by drilling holes in the side and drying it with compressed air.

#### 4.2.3.2 Different signal intensities REST slab suppressive and non-suppressive scan protocol

The non-suppressive and rest-slab suppressive scan had different signal intensities throughout the entire volume in the *no-motion* scans.

In the voxels in the acetone container, this is expected, as the REST slab suppresses signal in this region. However, it was also found that the signal intensity was lower in the REST slab suppressive scan in many of the voxels that do not contain the acetone container.

In part, this may be explained by a reduced influence of the acetone PSF. However, if this were the only reason, it would be expected that the signal would be more similar between the two scan protocols if the farthest voxels from the acetone container are considered. These voxels should contain the least acetone signal to begin with. This was not found to be the case, see Fig. 20.

The two scan protocols had a different repetition time ( $T_R$ ), see Section 4.2.3.3. This does not explain this observation.

The pulses were block pulses for both protocols, and for as far as it could be seen in the settings, there were no differences. Therefore, this also does not explain the observation.

The different signal intensities could also be due to some scaling somewhere in the reconstruction pipeline. However, this could not be verified, as there is very little insight in the exact reconstruction, see Section 4.2.3.5.

The difference in signal intensities may be caused by the fact that shimming and power optimization is repeated for every scan, see Section 4.2.3.3.

The conclusion that the REST slab suppressive sequence is effective in reducing the amount of ghosting can still be sufficiently substantiated with this data. The difference in signal intensities between the non-suppressive and REST slab suppressive scan is much higher in the *motion* scans than in the *no-motion* scans.

An intuitive solution would be to rescale the data to be of the same scale. However, this is challenging. It must be known what is the reason for the different intensities in the scans and what kind of effect this has on each location in the volume. An idea could be to rescale the data so that the average noise, defined as the standard deviation of the signal outside of the region where water or acetone is expected, is the same in both datasets. However, it is unclear if the the REST slab suppressive scan also has lower noise levels, or if it is only the peaks itself that are lower, while noise is still similar. If the noise is not the same in both scans, the amplifier settings may have changed between scans.

#### 4.2.3.3 Scan settings

The scan settings were not the same for the different protocols. The REST slab suppressive scan had a longer  $T_R$  than the non-suppressive protocol. If the  $T_R$  is insufficient for complete  $T_1$  relaxation of the subject, it is expected that a longer  $T_R$  would lead to more relaxation between excitations in the REST slab suppressive scan and therefore a higher signal. However, in practice, it was found that signal was higher in the non-suppressive scan in voxels that do not contain the acetone container. Therefore, the difference in scan settings is not a satisfactory explanation for this effect.

Before each scan, the scanner runs multiple short scans to optimize several parameters, such as power optimization and shimming. These may have led to different optimizations for every scan and could also contribute to the different signal intensities.

For an accurate comparison, it is recommended that the settings for any investigated pulses are made as equal as possible. The optimization should not be repeated for every scan.

#### 4.2.3.4 Imperfect shimming

For an explanation about shimming, see Section 1.1.2.2.

Due to imperfect shimming, which was also different for every scan, water residuals everywhere in the phantom are expected to have had a different resonance frequency. This explains the presence

of more than two peaks in the spectra. Because peaks could occur at several frequencies, it was not possible to investigate whether the ghosting artifact itself had shifts in frequency.

It was attempted to turn off shimming, so that all scans performed have the same shim settings and as identical as possible  $B_0$  and  $B_1$  (in)homogeneities. However, due to technical limitations this was not possible. The scanner was not able to export the data in the required format if shimming was turned off. This is expected to be due to a bug in the system, which was not prioritized to investigate further.

#### 4.2.3.5 Lack of control over reconstruction

3DiCSI was used, which made it very easy to inspect the data. However, this required the data to be exported as .SPAR/.SDAT, a data format in which a lot of processing had already been done. The use of this tool and this data format came at the cost of less control and knowledge over the reconstruction and what steps were precisely performed.

For example, the frequency axis in 3DiCSI is not shifted to display peaks at their actual calibrated location. Instead, 0 ppm is taken as the transmitter frequency. Moreover, it is not possible to change reconstruction steps related to denoising, which could have been used for clearer spectra, or implement any other processing steps such as water suppression.

Processing raw data using a custom pipeline allows for full control over every parameter and for the extraction of the maximum amount of information. However, this requires a lot of time and knowledge. The current setup was sufficient for showing the presence of the ghosting artifact and the reduction of ghosting due to the REST slab suppressive sequence.

#### 4.2.3.6 Definition of signal intensity

In this experiment, the signal intensity was defined as the maximum value of a spectrum. However, in MRSI, it is customary to integrate signals or fit concentrations [30]. However, these approaches are much more complex to use in these experiments than maximum value analysis.

The residual water in this experiment can have quite a wide range of peak locations due to magnetic field inhomogeneities. This leads to a range of combinations of peak locations that have to be accounted for if any kind of fitting would be performed, which is not feasible. Moreover, the location of the water peak is often very close to the acetone peak, making it very difficult to automatically determine if a peak corresponds to acetone or water. Integration is challenged by the fact that there is a non-horizontal baseline in the spectra, making it more difficult to isolate and quantify peaks.

A disadvantage of taking the maximum value is that it is sensitive to natural variance, as only 1 value of a spectrum is used.

A second disadvantage is that a random noise value may be selected if there is very low signal in a spectrum. In this experiment, there were no spectra observed where the signal was so low that this could happen.

A third disadvantage is that any peak height decrease accompanied by a linewidth increase will be considered to be a decrease in signal intensity, although the area under the peak, related to the concentration, may be the same.

The main advantages are that it is very easy to implement and that the functioning of the process can be easily verified, compared to fitting. It is sufficient for the analyses in this experiment, as the signal differences are so large that the added accuracy of more sophisticated methods are not expected to have led to a different conclusion.

#### 4.2.3.7 Voxel selection

As mentioned, it was observed that there was a clear signal in even the voxels with the lowest maximum value. This signal could have been generated by residual water and the PSF of the acetone container. As a result, there were no voxels that contain a fully noisy spectrum. Because only the maximum value of a spectrum is extracted, any effects of acetone ghosting could only be identified if these effects led to a new maximum value, meaning that the peak of the ghost was larger than any

peak already present. To maximize sensitivity to these kind of effects, the voxels with the 10% lowest maximum value in the *no-motion* scan were analyzed.

The choice of the percentage of 10% was a balance between sample size and presence of signal in the *no-motion* scan. Choosing a lower percentage yielded less influence of the already present signal, but also reduced the sample size. As there would always be some residual signal in the selected voxels, there was no clear cutoff value after which spectra suddenly worsened. Therefore, the exact choice would always remain arbitrary to some extent. The selection of the 10% voxels with lowest intensity consisted of 248 voxels, which was considered to be a sufficiently large sample size.

A first downside was that this method may have inherently increased the likelihood of an observation of a signal increase. It is expected that there is always some random variation in signal intensity between two identical scans. By selecting voxels with the lowest intensity, a slight bias is introduced in the selection to select voxels that had a lower-than-expected maximum value by chance. Therefore, a second scan is expected to have an average increase in signal intensity in the voxels. However, this effect was expected to be very minor. It was definitely smaller than the increase caused by ghosting, as the signal increased much more in the non-suppressive scan than in the REST slab suppressive scan.

A second downside was that any investigation into a spatial relationship in ghosting became very difficult. The 10% voxels were chosen solely based on their signal intensity and were scattered around the volume. The scattering of the voxels can be seen in Fig. 21 in Appendix A.2. It can be seen that the selected voxels were near the borders of the volume, which was also where the lowest signal is expected. To properly investigate a spatial relationship, however, it would be needed to investigate signals at several distances with the same sample size.

#### 4.2.3.8 Statistics

It was difficult to create a solid statistical basis on whether any differences in signal intensity were actually significant. This was mainly because each voxel could not be seen as an independent measurement, because adjacent voxels were subject to similar artifacts due to the point spread function. The Hann filter was expected to reduce the size of the PSF, but the water and acetone signal was still quite widely spread. Moreover, each experiment was only performed once, which meant that it was not possible to do statistics by comparing bulk values of several repetitions of the same experiment.

A possible solution for this would be to investigate voxels that are at least 2 voxels apart, which reduces the effects of the PSF a lot. A downside of this is that the sample size is reduced a lot.

Because they were only performed once, the inherently expected variance between two identical scans was unknown. Therefore, it was also not possible to say if differences between two scans could be explained by natural variance as well.

The found ghosting effects in this experiment were so large, that they are expected to be significant. To increase and actually quantify the significance of this observation, the experiment must be repeated multiple times. Moreover, to reduce the variance due to shimming and power optimization, these processes should only be performed once and their resulting parameters should be the same for every scan.

#### 4.2.3.9 Limited representation of in vivo situation

Experiment 3 showed that ghosting can occur due to objects with similar motion as the stomach, and that this ghosting can be reduced with a REST slab suppressive scan. However, the magnitudes of these effects cannot be related to the in vivo situation, as the amount of ghosting observed in the in vivo situation is not known. This makes it difficult to say to what extent the phantom replicates the artifacts observed in in vivo measurements. Moreover, it makes it difficult to say if any amount of ghosting reduction observed in phantom experiments is sufficient for the in vivo situation.

The expected amount of ghosting could be extracted from existing  $^2\text{H}$ -MRSI scans that exhibit the artifact by comparing the maximum  $^2\text{H}$ -glucose measured outside of the body to the voxel in the

stomach with the highest fitted  $^2H$ -glucose concentration. This could then be compared to the phantom by comparing the signal intensity in a voxel outside of the acetone container to the maximum signal intensity in the acetone container in the *motion* scan.

The used acetone container was 50mL. However, the stomach can have a filled volume of about 1100mL [56]. This difference in size could lead to a different amount of observed ghosting. Therefore, it is strongly recommended to use a bigger container that can change sizes to simulate different amounts of stomach filling.

#### 4.2.3.10 Slice selective protocol

In this project, but not included in this thesis, the effectiveness of a slice selective excitation sequence, positioned outside of the path of the moving container was researched as well. In the feasibility analysis, it was found that theoretically perfect separation of portal vein and stomach was possible with a slice selective technique as well.

The results of the phantom experiments with slice selection were difficult to interpret, due to challenges with inconsistent shimming, inconsistent power optimization and data with much lower signal values. A slice selective protocol is expected to be easier to implement and have more predictable effects than a REST slab suppressive protocol, as a slice selective protocol does not require an additional pulse [30]. It is recommended to consider investigating slice selective protocols as well in future research.

### 4.3 General discussion

#### 4.3.1 General remark regarding objective 2, 3 and 4 (In vivo 7T $^{31}P$ -MRSI)

The fact that the deep breathing datasets have much different results as the free breathing datasets in LW, SNR, CRLB, visual clarity and quantification repeatability, also supports that the free breathing datasets were acquired properly. There is no reason to assume that the lack of differences is due to errors, as clearly, it is possible to acquire data in which all these properties are worsened.

#### 4.3.2 General remark regarding objective 5 (Phantom simulation of ghosting)

This experiment yielded 3D visualizations of ghosting in MRSI, which, to the best knowledge of the author, have not yet been published in literature yet.

#### 4.3.3 Implications for current practice

This study aimed to investigate several challenges in  $^2H$ -MRSI for potential use as a quantitative function test for CMI. Specifically, it was investigated whether ghosting may be the reason for artifacts observed in currently performed  $^2H$ -MRSI studies in a proof-of-principle phantom study. This has shown that respiratory motion of the stomach may cause these artifacts. Moreover, it has been shown that a REST slab suppressive scan has the potential to reduce these artifacts. Another challenge that was investigated was the effect of respiratory motion on spectra. Currently, non-gated scans are performed in  $^2H$  - and  $^{31}P$  -MRSI. In this study, no evidence was found that this introduces a large error in  $^{31}P$ -MRSI in the liver.

The finding that gated acquisition may not be necessary in acquisition of large organs in free breathing patients may be valuable to all MRSI research done on liver tissue affected by respiratory motion.

Another valuable finding is that this study suggests that respiratory gating or methods to reduce breathing motion are valuable in scans of patients with deep respiratory motion.

#### 4.3.4 Future developments for $^2H$ -MRSI as an accessible function test for CMI

Previously, the focus of the experimental discussion has been on direct improvements and shortcomings of the current setups. There are also a few fundamentally different suggestions for experiments that focus on the same objectives of this thesis.

#### 4.3.4.1 Development directions for $^{31}\text{P}$ -MRSI as a substitute for $^2\text{H}$ -MRSI

An important difference between this study and scanning the portal vein is the fact that the portal vein is much smaller. This may make it more sensitive to motion, as voxels placed in the portal vein are more likely to contain a combination of different tissues as a result of respiratory motion. To use  $^{31}\text{P}$ -MRSI to better approximate expected effects on the portal vein, a small organ could be scanned, like the gall bladder.

The gall bladder actually has a very localized metabolite, phosphatidylcholine (PtdC) [57], which may be suitable as a surrogate for  $^2\text{H}$ -lactate in the portal vein. Moreover, as shown in this study, the gall bladder is subject to similar respiratory motion. It can have a different size and shape as the portal vein, but is in the same order of magnitude.

To properly interpret the results on PtdC in the gall bladder, the expected SNR of  $^2\text{H}$ -lactate in spectra in CMI must be known. If the SNR of  $^2\text{H}$ -lactate is very low, effects on PtdC may only be small for a conclusion that gating is not necessary. If the SNR of lactate is high, there is more room for spectral worsening and larger motion effects may be acceptable. This expected SNR is expected to be influenced by the sensitivity of the coils to  $^2\text{H}$ -lactate, the excitation efficiency and the concentration of  $^2\text{H}$ -lactate in the portal vein. This last factor is influenced by the lactate production of the ischemic bowels and by the concentration of  $^2\text{H}$ -glucose, which is used for the production of this  $^2\text{H}$ -lactate.

#### 4.3.4.2 Development directions for investigating ghosting

To make the experiment more representative of the actual  $^2\text{H}$ -MRSI setup, it would be valuable to investigate it further on 7T in in vivo experiments. It would be a minor addition to existing  $^2\text{H}$ -MRSI studies to add a single scan with slice selection or REST slab suppression. This would be the most effective way to investigate (the reduction of) ghosting in  $^2\text{H}$ -MRSI for this specific purpose. However, to do this, ethical permission should be granted and the total scan time should not be too long.

If in vivo experiments are not possible, or if it is desired to research different techniques in a very repeatable method, it is valuable to continue with phantom experiments. It is recommended to perform these experiments with 7T  $^2\text{H}$ -MRSI with  $^2\text{H}$ -containing compounds. This allows for a measurement setup that is as close as possible to the in vivo situation. Moreover, it is possible to investigate or improve the effectiveness of deuterium-specific ghosting reduction sequences.

An interesting improvement on the phantom would be to automate the the movement of the container. This allows for better repeatability and better comparability between scans. It also allows for longer scan times as no manual labor or attention of the operator is required, allowing for a larger grid size, repetition time or number of averages.

Designwise, it would be interesting to change the shape of the container. The stomach is shaped more like a ball, instead of a longitudinal container. A container that is larger in directions perpendicular to the object motion means that the time the container spends in a certain voxel is affected for more voxels, expectedly leading to more ghosting. Ideally, the container should also simulate peristaltic movement of the stomach [58].

The improved phantom could also be used on 1.5T  $^1\text{H}$ -MRSI, if it is preferred not to use 7T  $^2\text{H}$ -MRSI.

#### 4.3.4.3 Development directions for $^2\text{H}$ -MRSI

To develop  $^2\text{H}$ -MRSI as a function test for CMI, several other aspects, not related to respiratory motion, can be investigated.

##### Optimize scan time

It could be an interesting research direction to explore the balance between scan time and spectral quality. As the time between onset of symptoms and irreversible damage is limited in AMI [6], it is valuable to save as much time as possible.

##### Single voxel spectroscopy

Instead of performing multivoxel MRS using MRSI, it could be interesting to investigate single voxel

spectroscopy (SVS) [59]. The benefit of SVS is that it is possible to measure a higher quality spectrum in a shorter amount of time. However, as only 1 voxel is measured at a time, it is not possible to verify after acquisition whether actually the portal vein was measured, and it is much more difficult to do spatial analyses. For example, it will be challenging to investigate the speed by which  $^2H$ -glucose is converted to  $^2H$ -lactate and at which location this happens.

### **Flow**

In several master theses [15, 17], the impact of flow on the signal of lactate in  $^1H$ -MRSI has been studied at 7T. These experiments may have to be repeated for  $^2H$ -lactate at 7T. Ideally, a (non-urgent) CMI patient would be scanned at 7T with  $^2H$ -glucose, with and without gating. A positive result from this may increase developmental progress quickly and allow for more specifically designed experiments. If  $^2H$ -lactate is clearly visible despite flow conditions, flow experiments may be skipped and time and energy could be focused on development of other aspects, such as scan time reduction or ghosting reduction using  $^2H$ -REST slab suppressive or slice selective sequences.

### **Accessibility**

If, at some point in the future, all challenges are resolved at 7T, it will be an important step to increase accessibility to the test. An important step for this is to translate the methods to 3T. 7T scanners are quite rare and mostly exclusive to university medical centers. However, almost every hospital in the Netherlands has a 3T scanner. The translation of this technique to 3T greatly increases accessibility and may also increase the attention for the technique, leading to more research, faster improvements and commercial support. There are already experimental setups for  $^2H$ -MRSI at 3T [60, 61]. Moreover, in the context of central nervous lesions in the brain, some  $^2H$ -lactate has already been detected in the brain [60, 61]. Therefore, this translation may be feasible.

### **Pathologic lactate concentration**

If the development of a quantitative function test has been successful, it is needed to find a critical lactate concentration that can be classified as a pathological concentration. This can be done by studying healthy volunteers or CMI patients. To study this concentration in healthy volunteers, it can be used that exercise can induce mesenteric ischemia [11, 62]. If these volunteers ingested  $^2H$ -glucose before their exercise,  $^2H$ -lactate may be measurable in the portal vein. Moreover, CMI patients can be scanned to obtain spectra with pathologically realistic lactate peaks.

## 5 Conclusion

In this proof-of-principle study, no evidence was found that acquiring non-gated scans in volunteers with regular breathing affects the subjective quality, objective quality or quantification of liver  $^{31}\text{P}$ -MRSI spectra. However, the subjective and objective quality and repeatability of quantification worsened tremendously in liver  $^{31}\text{P}$ -MRSI scans with deep breathing. Therefore, measures should be taken for scans of deep breathing patients. Further research is required to confirm whether these findings are applicable to  $^2\text{H}$ -MRSI in the portal vein.

This proof-of-principle study demonstrated in a phantom simulation that respiratory motion of the stomach may cause a large signal increase in voxels outside of the stomach due to ghosting. Therefore, it is plausible that respiratory motion in the stomach could lead to ghosting artifacts in  $^2\text{H}$ -MRSI. The phantom experiment also showed that a REST slab suppressive protocol can be very effective in reducing these artifacts. Therefore, it is likely that ghosting artifacts in  $^2\text{H}$ -MRSI can be reduced using a REST slab suppressive protocol.

---

## References

- [1] Luke G Terlouw et al. “European guidelines on chronic mesenteric ischaemia–joint United European Gastroenterology, European Association for Gastroenterology, Endoscopy and Nutrition, European Society of Gastrointestinal and Abdominal Radiology, Netherlands Association of Hepatogastroenterologists, Hellenic Society of Gastroenterology, Cardiovascular and Interventional Radiological Society of Europe, and Dutch Mesenteric Ischemia Study group clinical guidelines on the diagnosis and treatment of patients with chronic mesenteric ischaemia”. In: *United European gastroenterology journal* 8.4 (2020), pp. 371–395. doi: 10.1177/2050640620916681.
- [2] Luke G Terlouw et al. “The incidence of chronic mesenteric ischemia in the well-defined region of a Dutch mesenteric ischemia expert center”. In: *Clinical and translational gastroenterology* 11.8 (2020), e00200. doi: 10.14309/ctg.000000000000200.
- [3] Eric J Hohenwalter. “Chronic mesenteric ischemia: diagnosis and treatment”. In: *Seminars in interventional radiology*. Vol. 26. 04. © Thieme Medical Publishers. 2009, pp. 345–351. doi: 10.1055/s-0029-1242198.
- [4] Martin Björck et al. “Editor’s choice–management of the diseases of mesenteric arteries and veins: clinical practice guidelines of the European Society of Vascular Surgery (ESVS)”. In: *European Journal of Vascular and Endovascular Surgery* 53.4 (2017), pp. 460–510. doi: 10.1016/j.ejvs.2017.01.010.
- [5] Aurora Lemma et al. “Editor’s Choice–Epidemiology, Diagnostics, and Outcomes of Acute Occlusive Arterial Mesenteric Ischaemia: A Population Based Study”. In: *European Journal of Vascular and Endovascular Surgery* 64.6 (2022), pp. 646–653. doi: 10.1016/j.ejvs.2022.07.006.
- [6] Ernst Klar et al. “Acute mesenteric ischemia: a vascular emergency”. In: *Deutsches Ärzteblatt International* 109.14 (2012), p. 249. doi: 10.3238/arztebl.2012.0249.
- [7] Peter BF Mensink, Leon MG Moons, and Ernst J Kuipers. “Chronic gastrointestinal ischaemia: shifting paradigms”. In: *Gut* 60.5 (2011), pp. 722–737. doi: 10.1136/gut.2009.199695.
- [8] Kim Van Wijck et al. “Exercise-induced splanchnic hypoperfusion results in gut dysfunction in healthy men”. In: *PloS one* 6.7 (2011), e22366. doi: 10.1371/journal.pone.0022366.
- [9] Juliëtte Blauw. “Optimizing outcome and quality of life for mesenteric ischemia patients by improving diagnostic and treatment strategies”. In: (2022). doi: 10.3990/1.9789036553278.
- [10] Daniel G Clair and Jocelyn M Beach. “Mesenteric ischemia”. In: *New England Journal of Medicine* 374.10 (2016), pp. 959–968. doi: 10.1056/NEJMra1503884.
- [11] Desirée van Noord and Jeroen J Kolkman. “Functional testing in the diagnosis of chronic mesenteric ischemia”. In: *Best practice & research Clinical gastroenterology* 31.1 (2017), pp. 59–68. doi: 10.1016/j.bpg.2016.12.002.
- [12] Joep PM Derikx, Dirk HSM Schellekens, and Stefan Acosta. “Serological markers for human intestinal ischemia: A systematic review”. In: *Best practice & research Clinical gastroenterology* 31.1 (2017), pp. 69–74. doi: 10.1016/j.bpg.2017.01.004.
- [13] E.N. Marieb and K.N. Hoehn. *Human Anatomy & Physiology*. Pearson Education, 2015. isbn: 9780133995190. url: <https://books.google.nl/books?id=ac2gBwAAQBAJ>.
- [14] P K J D De Jonge B et al. “Non invasive measurement of lactate in whole blood using nuclear magnetic resonance spectroscopy as a diagnostic tool in chronic splanchnic ischemia”. In: (2011).
- [15] S Cnossen et al. “Diagnosis of mesenteric ischemia using magnetic resonance spectroscopy Refocused double-quantum editing for lactate detection in the portal vein”. In: (2019).
- [16] Kevin Reijnen. “Double quantum coherence editing for lactate detection as a potential functional test for mesenteric ischemia at 7T”. In: (2021).
- [17] Xijing Zhang. “Diagnosis of Mesenteric Ischemia with 1 H MR Spectroscopy The measurement of lactate in the portal vein with multiple inversion recovery”. In: (2021).
- [18] Henk M De Feyter and Robin A de Graaf. “Deuterium metabolic imaging–Back to the future”. In: *Journal of Magnetic Resonance* 326 (2021), p. 106932. doi: 10.1016/j.jmr.2021.106932.

- 
- [19] Muhammad G. Saleh et al. "Motion correction in magnetic resonance spectroscopy". In: *Magnetic Resonance in Medicine* 84 (5 Nov. 2020), pp. 2312–2326. issn: 0740-3194. doi: 10.1002/mrm.28287.
- [20] Aaron T. Hess et al. "Real-time motion and B 0 corrected single voxel spectroscopy using volumetric navigators". In: *Magnetic Resonance in Medicine* 66 (2 Aug. 2011), pp. 314–323. issn: 0740-3194. doi: 10.1002/mrm.22805.
- [21] J Felblinger, R Kreis, and C Boesch. "Effects of physiologic motion of the human brain upon quantitative 1H-MRS: analysis and correction by retro-gating". In: *NMR in Biomedicine: An International Journal Devoted to the Development and Application of Magnetic Resonance In Vivo* 11.3 (1998), pp. 107–114. doi: 10.1002/(sici)1099-1492(199805)11:3<107::aid-nbm525>3.0.co;2-i.
- [22] Woutjan Branderhorst et al. *The effect of respiratory motion on in vivo 31P magnetic resonance spectroscopic imaging in the human liver at 7 Tesla*. 2024.
- [23] Leonard WF Seelen et al. "31P MR spectroscopy in the pancreas: Repeatability, comparison with liver, and pilot pancreatic cancer data". In: *Journal of Magnetic Resonance Imaging* 60.6 (2024), pp. 2657–2666. doi: 10.1002/jmri.29326.
- [24] Quincy van Houtum et al. "Low SAR 31P (multi-echo) spectroscopic imaging using an integrated whole-body transmit coil at 7T". In: *NMR in Biomedicine* 32.12 (2019), e4178. doi: 10.1002/nbm.4178.
- [25] J Löring et al. "Whole-body radiofrequency coil for 31P MRSI at 7 T". In: *NMR in biomedicine* 29.6 (2016), pp. 709–720. doi: 10.1002/nbm.3517.
- [26] Quincy ( Q) van Houtum et al. "Feasibility of 31P spectroscopic imaging at 7 T in lung carcinoma patients". In: *NMR in Biomedicine* 34.5 (2021), e4204. doi: 10.1002/nbm.4204.
- [27] Roma Pahwa and Ishwarlal Jialal. *Atherosclerosis*. 2025.
- [28] Richard A Watts et al. "Global epidemiology of vasculitis". In: *Nature reviews rheumatology* 18.1 (2022), pp. 22–34. doi: 10.1038/s41584-021-00718-8.
- [29] Lars G Hanson. "Is quantum mechanics necessary for understanding magnetic resonance?" In: *Concepts in Magnetic Resonance Part A: An Educational Journal* 32.5 (2008), pp. 329–340. doi: 10.1002/cmr.a.20123.
- [30] Robin A.. De Graaf. *In Vivo NMR Spectroscopy : Principles and Techniques*. Wiley-Interscience, 2008. isbn: 9780470026700.
- [31] Stefan Posse et al. "MR spectroscopic imaging: principles and recent advances". In: *Journal of Magnetic Resonance Imaging* 37.6 (2013), pp. 1301–1325. doi: 10.1002/jmri.23945.
- [32] Richard L Ehman et al. "Magnetic resonance imaging with respiratory gating: techniques and advantages". In: *American journal of Roentgenology* 143.6 (1984), pp. 1175–1182. doi: 10.2214/ajr.143.6.1175.
- [33] AJ Schwarz and MO Leach. "Implications of respiratory motion for the quantification of 2D MR spectroscopic imaging data in the abdomen". In: *Physics in Medicine & Biology* 45.8 (2000), p. 2105. doi: 10.1088/0031-9155/45/8/304.
- [34] VL Doyle, FA Howe, and JR Griffiths. "The effect of respiratory motion on CSI localized MRS+ ". In: *Physics in Medicine & Biology* 45.8 (2000), p. 2093. doi: 10.1088/0031-9155/45/8/303.
- [35] Joel P Felmler and Richard L Ehman. "Spatial presaturation: a method for suppressing flow artifacts and improving depiction of vascular anatomy in MR imaging." In: *Radiology* 164.2 (1987), pp. 559–564.
- [36] Leentje Vanhamme, Aad van den Boogaart, and Sabine Van Huffel. "Improved Method for Accurate and Efficient Quantification of MRS Data with Use of Prior Knowledge". In: *Journal of Magnetic Resonance* 129.1 (1997), pp. 35–43. issn: 1090-7807. doi: [https : / / doi . org / 10 . 1006 / jmre . 1997 . 1244](https://doi.org/10.1006/jmre.1997.1244). url: <https://www.sciencedirect.com/science/article/pii/S1090780797912441>.
- [37] Leentie Vanhamme et al. "MR spectroscopy quantitation: a review of time-domain methods". In: *NMR in Biomedicine: An International Journal Devoted to the Development and Application of Magnetic Resonance In Vivo* 14.4 (2001), pp. 233–246. doi: 10.1002/nbm.695.
- [38] Roland Kreis. "Issues of spectral quality in clinical 1H-magnetic resonance spectroscopy and a gallery of artifacts". In: *NMR in Biomedicine* 17.6 (2004), pp. 361–381. doi: 10.1002/nbm.891.
-

- 
- [39] Lieke van den Wildenberg et al. "In vivo phosphorus magnetic resonance spectroscopic imaging of the whole human liver at 7 T using a phosphorus whole-body transmit coil and 16-channel receive array: Repeatability and effects of principal component analysis-based denoising". In: *NMR in Biomedicine* 36.5 (2023), e4877. doi: 10.1002/nbm.4877.
- [40] Roland Kreis et al. "Terminology and concepts for the characterization of in vivo MR spectroscopy methods and MR spectra: background and experts' consensus recommendations". In: *NMR in Biomedicine* 34.5 (2021), e4347. doi: 10.1002/nbm.4347.
- [41] Henk M. De Feyter and Robin A. de Graaf. "Deuterium metabolic imaging – Back to the future". In: *Journal of Magnetic Resonance* 326 (2021), p. 106932. issn: 1090-7807. doi: <https://doi.org/10.1016/j.jmr.2021.106932>. url: <https://www.sciencedirect.com/science/article/pii/S1090780721000215>.
- [42] S Müller and J Seelig. "In vivo NMR imaging of deuterium". In: *Journal of Magnetic Resonance* (1969) 72.3 (1987), pp. 456–466. doi: 10.1016/0022-2364(87)90150-8.
- [43] Guido Van Rossum and Fred L. Drake. *Python 3 Reference Manual*. Scotts Valley, CA: CreateSpace, 2009. isbn: 1441412697.
- [44] Lieke van den Wildenberg et al. "Measurement of metabolite levels and treatment-induced changes in hepatic metastases of gastro-esophageal cancer using 7-T phosphorus magnetic resonance spectroscopic imaging". In: *NMR in Biomedicine* (2024), e5155. doi: 10.1002/nbm.5155.
- [45] Martijn Froeling et al. "PCA denoising and Wiener deconvolution of 31P 3D CSI data to enhance effective SNR and improve point spread function". In: *Magnetic resonance in medicine* 85.6 (2021), pp. 2992–3009. doi: 10.1002/mrm.28654.
- [46] Peter B Roemer et al. "The NMR phased array". In: *Magnetic resonance in medicine* 16.2 (1990), pp. 192–225. doi: 10.1002/mrm.1910160203.
- [47] J Martin Bland and Douglas G Altman. "Statistical methods for assessing agreement between two methods of clinical measurement". In: *The lancet* 327.8476 (1986), pp. 307–310. doi: 10.1016/S0140-6736(86)90837-8.
- [48] Xiaoke Wang, Scott B Reeder, and Diego Hernando. "An acetone-based phantom for quantitative diffusion MRI". In: *Journal of Magnetic Resonance Imaging* 46.6 (2017), pp. 1683–1692. doi: 10.1002/jmri.25727.
- [49] Qi Zhao et al. "An interactive software for 3D chemical shift imaging data analysis and real time spectral localization and quantification". In: *Proc Int Soc Mag Reson Med*. Vol. 13. 2005, p. 2465.
- [50] Katja M Langen and Dan TL Jones. "Organ motion and its management". In: *International Journal of Radiation Oncology\* Biology\* Physics* 50.1 (2001), pp. 265–278. doi: 10.1016/S0360-3016(01)01453-5.
- [51] Barbara Wysocka et al. "Interfraction and respiratory organ motion during conformal radiotherapy in gastric cancer". In: *International Journal of Radiation Oncology\* Biology\* Physics* 77.1 (2010), pp. 53–59. doi: 10.1016/j.ijrobp.2009.04.046.
- [52] Patrick Chau et al. "A systematic review and meta-analysis of portal vein morphometry in pediatric and adult populations: drawing the line between normal and abnormal findings". In: *European Journal of Radiology* 168 (2023), p. 111016. doi: 10.1016/j.ejrad.2023.111016.
- [53] Patrick S Kamath and Vijay H Shah. "Portal hypertension related to bleeding". In: *Zakim and Boyer's Hepatology: A Textbook of Liver Disease*. Elsevier, 2017, pp. 233–261. doi: 10.1016/B978-0-323-37591-7.00016-1.
- [54] G Nadeem. "A study of the clinico-anatomical variations in the shape and size of gallbladder". In: *Journal of Morphological Sciences* 33.02 (2016), pp. 062–067. doi: 10.4322/jms.082714.
- [55] Kigundu Yason et al. "Anatomical variations of the gallbladder and bile ducts: an MRI study". In: *International Journal of Hepatology* 2024.1 (2024), p. 3877814. doi: 10.1155/2024/3877814.
- [56] Attila Csendes and Ana Maria Burgos. "Size, volume and weight of the stomach in patients with morbid obesity compared to controls". In: *Obesity surgery* 15.8 (2005), pp. 1133–1136. doi: 10.1381/0960892055002158.
- [57] Alessandra Bierwagen et al. "Characterization of the peak at 2.06 ppm in 31P magnetic resonance spectroscopy of human liver: phosphoenolpyruvate or phosphatidylcholine?" In: *NMR in Biomedicine* 28.7 (2015), pp. 898–905. doi: 10.1002/nbm.3323.
-

- 
- [58] Anthony O'Connor and Colm O'Moráin. "Digestive function of the stomach". In: *Digestive diseases* 32.3 (2014), pp. 186–191. doi: 10.1159/000357848.
- [59] Yue Zhang et al. "Comparison of reproducibility of single voxel spectroscopy and whole-brain magnetic resonance spectroscopy imaging at 3T". In: *NMR in Biomedicine* 31.4 (2018), e3898. doi: 10.1002/nbm.3898.
- [60] Philip M Adamson et al. "Deuterium metabolic imaging for 3D mapping of glucose metabolism in humans with central nervous system lesions at 3T". In: *Magnetic resonance in medicine* 91.1 (2024), pp. 39–50. doi: 10.1002/mrm.29830.
- [61] Nikolaj Bøgh et al. "Repeatability of deuterium metabolic imaging of healthy volunteers at 3 T". In: *European Radiology Experimental* 8.1 (2024), p. 44. doi: 10.1186/s41747-024-00426-4.
- [62] Johannes A Otte et al. "Exercise induces gastric ischemia in healthy volunteers: a tonometry study". In: *Journal of Applied Physiology* 91.2 (2001), pp. 866–871. doi: 10.1152/jappl.2001.91.2.866.



### A.1 Similarity of in vivo $^3\text{P}$ -MRSI to literature [39]

It can be seen that the SNR of these measurements is lower than the reference article. Due to the normalization of the metabolite concentrations to a total of 100%, it is expected that any SNR-related scaling is compensated and therefore has limited influence. The lower SNR may still lead to higher variability in fitted concentrations. As in this thesis no clear increase in variability was found, so if the SNR would lead to a higher variability, it only supports the finding that a gated and non-gated scan are as similar as two non-gated scans.

**Table 15:** The SNR is lower in the performed measurements than in the article used for comparison.  $G_F$  - gated, free breathing;  $NG_F$  - non-gated, free breathing;  $NG_D$  - non-gated, deep breathing.

SNR (-)	$G_F$	$NG_F$	$NG_D$
V1	$13.5 \pm 4.4$	$12.8 \pm 4.9$	
V2	$12.9 \pm 3.4$	$12.2 \pm 3.5$	
V3	$18.3 \pm 5.3$	$18 \pm 5.8$	$10.1 \pm 4.7$
V4	$16.2 \pm 4.4$	$16.3 \pm 4.8$	$12.2 \pm 4.7$
V5	$13.8 \pm 3.6$	$16.9 \pm 4.0$	$10.5 \pm 3.9$
V6	$17.7 \pm 4.6$	$18.6 \pm 5.1$	$12.2 \pm 3.2$
$\mu \pm \sigma$	$15.4 \pm 2.3$	$15.8 \pm 2.7$	$11.2 \pm 1.1$
Literature [39] $\mu \pm \sigma$		$25.6 \pm 3.1$	
		$25.0 \pm 3.6$	

## A.2 Location of subselection of voxels in experiment 2

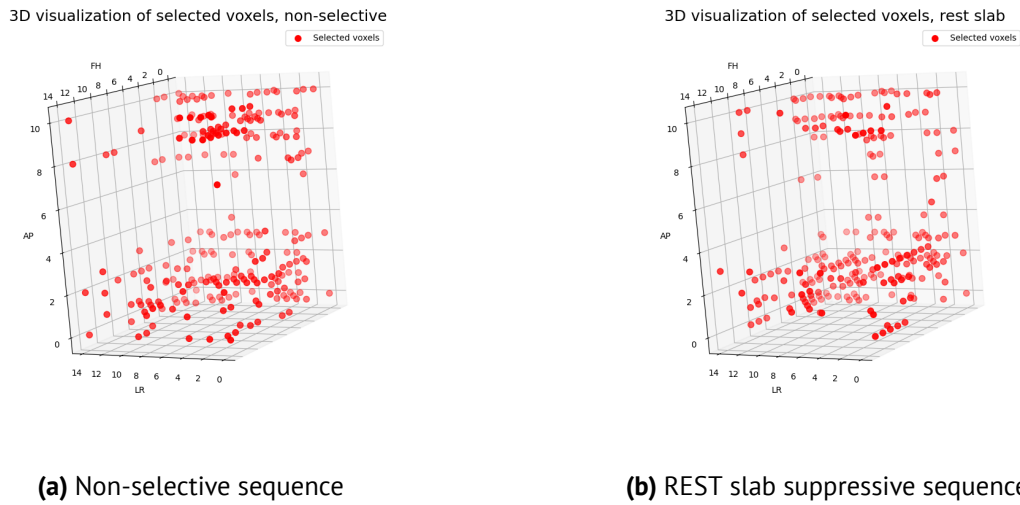


**Figure 21:** The locations of the subselection of voxels used for analysis in the non-suppressive and REST slab suppressive scans of the phantom experiment. The 10% voxels with the lowest signal intensity in the *no motion* scan are selected. It can be seen that the selected voxels are located near the borders of the volume in both scan sequences, and that the region with the acetone container contains no voxels.

---

# B Lists

## B.1 List of Figures

1	An example of suspected ghosting in a $^2H$ -MRSI study. It can be seen that signal is reconstructed in several areas outside of the body. Courtesy of Jeanine Prompers, UMC Utrecht. . . . .	6
2	The anatomy of the arterial mesenteric circulation [1]. The coeliac artery (CA) perfuses liver, spleen, pancreas, stomach and part of the duodenum. The superior mesenteric artery (SMA) perfuses part of the duodenum, the jejunum, ileum, ascending colon and the largest part of the transverse colon. The inferior mesenteric artery (IMA) perfuses the rest of the transverse colon, the descending colon, sigmoid and rectum. These three arteries are connected by a large network of collaterals. . . . .	8
3	Left: a typical PSF. Note the side lobes, decreasing in height, that represent the signal spreading to neighbouring voxels. Right: The effect of a Hamming filter on the PSF. Notice that the main lobe is wider and lower, and that the sidelobes have almost disappeared. Modified from [30]. . . . .	10
4	The experimental setup for experiment 1 at the 1.5T scanner with a volunteer out of the bore. The abdominal coil is placed on the thorax. The volunteer was positioned feet first. . . . .	13
5	Measurement setup of in vivo MRSI scans at 7T. The coils were placed below and on top of the thorax. The air bag of the respiratory sensor was placed on the stomach using a belt. The respiratory sensor itself was placed between the legs. Volunteers were positioned feet first. . . . .	15
6	Schematic overview of the box breathing pattern used to guide the subject in performing a consistent deep breathing pattern. Color guidance was used for three of the four subjects and an audio signal for one of the four subjects. . . . .	17
7	Example of a spectrum with visually distinctive peaks in the free breathing spectra and no distinctive peaks in the deep breathing spectra. These spectra are shifted based on the $\alpha$ -ATP peak. In this example, the free breathing (FB) spectra are of acceptable quality based on every mentioned criterion, whereas the deep breathing spectrum (DB) is of low quality in every mentioned criterion. . . . .	19
8	Overviews of the setup for the phantom experiment to simulate ghosting and investigate the reduction of ghosting via a REST slab suppressive sequence. . . . .	21
9	Visualization of free and deep respiration made with MRI at 1.5T. The arrows represent the movement along one axis, averaged over 3 volunteers, in free breathing. The striped line represents an ellipse with, along the axes, a radius of twice the standard deviation of the movement. The values that describe these arrows and ellipses are tabulated in Table 7. The background scans are of a free breathing volunteer, chosen because the structures are well defined in the imaged slices. Left: coronal views. Here, the portal vein is marked at the hilus (red) and near the spine (blue) Moreover, the top of the stomach, at the diaphragm, is marked (yellow). Right: Sagittal views. Here, the portal vein (red) and gall bladder (blue) are marked. Top: Free breathing. Bottom: Deep breathing. These figures show that, visually, in free breathing, all marked structures have similar feet-head motion. In deep breathing, the structures also have similar respiratory motion, visually, except for the portal vein near the hilus. This structure is subject to less motion. . . . .	24

---

10	The voxels that were marked as having spectra with poorly distinguishable peaks. Green voxels were marked in both the gated and non-gated free breathing scan. The pink voxel was only marked in the non-gated free breathing scan. The blue voxel was only marked in the gated free breathing scan. It can be seen that all of these voxels are located at the border of the liver. These voxels are more likely to have large differences in their contents due to motion, expectedly leading to worse spectra. . . . .	27
11	3D visualizations of the voxels of which the overall spectrum was judged as low and acceptable quality. It was opted to do a 3D visualization, as this gives a more intuitive feeling about the spatial location of low quality voxels than a collection of maps. It can be seen that the low quality voxels are all located posterior and in the direction of the head, mainly in the 4 coronal slices near the head. . . . .	28
12	The average and standard deviation of the 6 scanned volunteers. Legend: $G_F$ - gated, free breathing; $NG_F$ - non-gated, free breathing; $NG_D$ - non-gated, deep breathing. . .	29
13	The distributions of the voxelwise differences in linewidth for all volunteers. Values that are outside of the interval $[-100, 100]$ are binned in the bins on the outer edges. The different heights of the distribution can be explained by the different amount of voxels in the volunteers, as they all had different liver sizes. It can be seen that the average difference between gated and non-gated free breathing is not consistently positive or negative across the volunteers. Moreover, the difference distributions for both <i>gated free breathing - non-gated deep breathing</i> and for <i>non-gated free breathing - non-gated deep breathing</i> have a similar shape in each volunteer, indicating that the differences between free breathing and deep breathing are much larger than differences between gated and non-gated free breathing. It can also be seen that the difference distributions for <i>free breathing - deep breathing</i> contain mostly negative values. This indicates that for a voxel in a deep breathing scan, generally, a higher linewidth is fitted than for the same voxel in a free breathing scan. . . . .	31
14	The distributions of the voxelwise differences in SNR for all volunteers. Values that are outside of the interval $[-10, 10]$ are binned in the bins on the outer edges. The different heights of the distribution can be explained by the different amount of voxels in the volunteers, as they all had different liver sizes. It can be seen that the average difference between gated and non-gated free breathing is not consistently positive or negative across the volunteers. V5 is an outlier in these comparisons, with overall lower SNR for the non-gated free breathing dataset than for the gated free breathing dataset. The shape of the difference distributions for both <i>gated free breathing - non-gated deep breathing</i> and for <i>non-gated free breathing - non-gated deep breathing</i> have a similar shape in each volunteer, indicating that the differences between free breathing and deep breathing are much larger than differences between gated and non-gated free breathing. It can also be seen that the difference distributions for <i>free breathing - deep breathing</i> contain mostly negative values. This indicates that for a voxel in a deep breathing scan, generally, a lower SNR is determined than for the same voxel in a free breathing scan. . . . .	32

15	The distributions of the voxelwise differences in CRLB of $\alpha$ -ATP for all volunteers. Values that are outside of the interval [-10,10] are binned in the bins on the outer edges. The different heights of the distribution can be explained by the different amount of voxels in the volunteers, as they all had different liver sizes. In the calculations of mean and standard deviations, CRLB's over 100% have been dismissed, see Section 2.2.6. Number of dismissed values: $G_F - NG_F$ , $0.3 \pm 0.8$ values; $G_F - NG_D$ , $9.3 \pm 9.2$ ; $NG_F - NG_D$ , $9 \pm 9.3$ . It can be seen that the average difference between gated and non-gated free breathing is not consistently positive or negative across the volunteers. Moreover, the difference distributions for both <i>gated free breathing - non-gated deep breathing</i> and for <i>non-gated free breathing - non-gated deep breathing</i> have a similar shape in each volunteer, indicating that the differences between free breathing and deep breathing are much larger than differences between gated and non-gated free breathing. The average difference is much larger for the <i>free breathing - deep breathing</i> comparisons than for <i>(non)-gated free breathing</i> comparisons. The <i>free breathing - deep breathing</i> distributions contain mostly negative values, indicating that for a voxel in a deep breathing scan, generally, a higher CRLB is fitted than for the same voxel in a free breathing scan. . . . .	33
16	Green: outline of portal vein. Blue: outline of liver. Red: outline of an area which could be selectively suppressive with a perfect REST slab. The slice is positioned so that the stomach does not leave the desired region during respiratory motion. Based on visual judgment, the sequence can be positioned so that the portal vein is unaffected, in the case of perfect selectivity. The liver cannot be completely separated from the stomach using an ideal rest slab suppressive sequence, but the largest part of the liver can be spared. . . . .	36
17	The signal in the voxels with the lowest signal intensity in the <i>no-motion</i> scan in the non-suppressive and the REST slab suppressive scans. Note the independent y-axes. The x-axis is calibrated with the transmit frequency at 0 ppm. It can be seen that in the voxel with the lowest signal, the signal is still larger than the noise for both acquisitions. Moreover, it can be seen that the signal increases about 40 times in the non-suppressive scan with the moving container, and only about 2 times in the rest-slab scans. . . . .	37
18	The signal intensities of the same slice of every performed scan. The display limits are set to be $\pm$ (99 <sup>th</sup> percentile of absolute values), taken over all 4 datasets together. It can be seen that the maximum signal intensities are much lower in the REST slab scan than in the non-suppressive scan. However, subtle differences cannot be seen in this scaling. Fig. 19a shows the difference in intensities between the datasets in the top row. Fig. 20 shows the difference in intensities between the top row and the bottom row. The reference position of the container can be seen in Fig. 19b. Movement is from top to bottom. Units are arbitrary. . . . .	38
19	The difference in signal intensity between two regular <sup>1</sup> H-MRSI scans with a moving and a stationary acetone container. . . . .	39
20	The difference in intensity per voxel of the non-suppressive scan and the REST slab suppressive scan. The intensity has arbitrary units. It can be seen that in both the <i>no-motion</i> and <i>motion</i> dataset, the signal at the location of the acetone container is higher in the non-suppressive scan. In the <i>no-motion</i> datasets, the signal is generally higher in the non-suppressive dataset than in the REST slab suppressive dataset. In the <i>motion</i> datasets, the signal is much higher in the non-suppressive dataset than in the REST slab suppressive dataset. Also, in some of the regions where the REST slab suppressive signal was higher than the non-suppressive signal in the <i>no-motion</i> set, the signal is now also much higher in the non-suppressive scan. It can be seen that the difference in signal intensities in the areas without the acetone container is much larger in the <i>no-motion</i> dataset than in the <i>motion</i> dataset. The blue area is likely due to residual water. . . . .	40

---

21	The locations of the subselection of voxels used for analysis in the non-suppressive and REST slab suppressive scans of the phantom experiment. The 10% voxels with the lowest signal intensity in the <i>no motion</i> scan are selected. It can be seen that the selected voxels are located near the borders of the volume in both scan sequences, and that the region with the acetone container contains no voxels. . . . .	61
----	--	----

---

## B.2 List of Tables

1	All abbreviations used in this thesis. . . . .	3
1	All abbreviations used in this thesis. . . . .	4
2	The population of the volunteers for the in vivo motion and organ size measurements. . . . .	13
3	The scan settings used for scanning the volunteers. For FOV, voxel size and # voxels, the numbers represent respectively the AP, RL, FH direction. All scans are a balanced FFE scan. The precise echo and repetition time vary slightly between scan protocols, likely due to automatic optimization by the scanner. The transversal scan was not used for motion measurements, as no full cycle could be seen of any marked structure as motion was primarily perpendicular to the scan plane. . . . .	14
4	The characteristics of the volunteer population for the <sup>31</sup> P-MRSI scans. . . . .	15
5	Acquired <sup>31</sup> P-MRSI scans. The values for FOV and Voxel size represent respectively AP, RL, FH. For the <sup>31</sup> P-MRSI scans, Hamming weighted acquisition was acquired with ten averages. The deep breathing scans were implemented later in time, which is why these were only acquired for 4 volunteers. . . . .	16
6	Scan settings of the phantom experiment. The $T_R$ is different between the two scans. Both scans are <sup>1</sup> H-MRSI scans. . . . .	22
7	Difference between maximum and minimum marked point during MRI scans at 1.5 of respiration. AP = anterior-posterior direction, LR = left-right direction, FH = feet-head direction. The portal vein in deep breathing in the coronal view was often not visible within the same plane due to imperfect plane positioning, so these values may be an underestimation of the actual respiratory motion. Any part of the portal vein that was visible in these views was marked if the target structure was not visible. As a result, LR movement may be overestimated for the portal vein in the coronal view in deep breathing. For the motion measurement of the stomach at the diaphragm, the focus was on measuring the feet-head motion at the most superior part. Therefore, the LR motion may be less accurate. The marked free breathing structures all have similar motion, as the maximum difference between the averages is 5 mm between the stomach and portal vein in the sagittal view. In deep breathing, the structures also have similar respiratory motion, except for the portal vein near the hilus, as the maximum difference in amplitude between the other structures is 10.2 mm. . . . .	25
8	Measured free breathing and deep breathing in the volunteers scanned for in vivo MRSI at 7T. Motion is measured as the maximum difference in FH locations of the diaphragm. It can be seen that in most volunteers, the motion of the diaphragm is much larger in deep breathing than in free breathing, as expected. V1 had very a very similar amount of motion in both free breathing and deep breathing. For V1, the deep breathing amplitude is similar to the other volunteers, but the free breathing amplitude is quite large. There is quite a large variation in observed breathing amplitudes. Generally, the determined breathing motion for the diaphragm in these measurements is larger than the determined breathing motion in the 1.5T MRI measurements (Table 7). . . . .	26
9	The percentage of spectra judged as low quality for every criterion in the 3 datasets of V3. . . . .	26
10	Coefficients of repeatability (CR) for several combinations of datasets, both absolute and relative to the average value in the respective combination of datasets. Values are marked green if they are lower (<) than the literature value, blue if they are equal (=) red if they are larger (>). It can be seen that the coefficients of repeatability are lower than the literature values much more often for the combination with free breathing datasets than for combinations with the deep breathing dataset, both when expressed absolutely and relatively. . . . .	34

---

11	Biases of several combinations of datasets. (Relative) biases with an absolute value smaller (<) than the reference are marked green, biases with the same absolute value (=) are marked blue, biases with an absolute value larger (>) than the reference are marked red. Relative biases are calculated as a percentage of the average fitted concentration. It can be seen that about half of the biases are smaller and half are larger than the reference for the combinations of the free breathing datasets. This means that on average, the difference in average fitted concentration is similar to values in literature. For comparisons with a deep breathing dataset, biases are generally much larger. This means that the difference in the average fitted values between the deep breathing dataset and free breathing sets is larger than between the gated and non-gated free breathing dataset. Biases are not generally signed positive or negative across metabolites in any of the combinations, due to the normalization of metabolite concentrations to a total of 100% (see Section 4.2.2.2). The sum of all absolute biases of all fitted metabolites, excluding PME, PDE and PME/PDE is 0 for every comparison. Abbreviations: $G_F$ , gated free breathing; $NG_F$ , non-gated free breathing; $NG_D$ , non-gated deep breathing. . . . .	35
12	The ratio of $\frac{motion}{no-motion}$ of the sum of the signal in the 10% voxels with the lowest <i>no-motion</i> signal. The signal increase in the scan with the moving acetone container is much greater in the non-suppressive scan compared to the REST slab suppressive scan, indicating that the REST slab suppressive scan experiences less ghosting, as expected. . . . .	40
13	The maximum signal intensity in the <i>no-motion</i> scans of both the non-suppressive and REST slab suppressive scan. The same voxel in the acetone container is chosen in the non-suppressive and REST slab suppressive scan, which has the maximum signal intensity in the <i>no-motion</i> scan in both datasets. The units are arbitrary. It can be seen that the maximum signal intensity is 20.5 times lower in the REST slab suppressive scan than in the non-suppressive scan. . . . .	40
14	Subjective judgments of the quality of spectra of volunteer V3. The column <i>S</i> contains subjective judgments whether the overall spectrum contained distinctive peaks. The column <i>P</i> contains subjective judgements whether the PME & PDE peaks were visually distinctive. The column $\gamma$ contains subjective judgments whether the $\gamma$ -ATP peak was distinctive. A 1 means that it was judged as <i>acceptable quality</i> , a 0 means that it was judged as <i>low quality</i> . The columns are grouped as <i>G, FB</i> (gated, free breathing), <i>NG, FB</i> (non-gated, free breathing) and <i>NG, DB</i> (non-gated, deep breathing). . . . .	59
15	The SNR is lower in the performed measurements than in the article used for comparison. $G_F$ - gated, free breathing; $NG_F$ - non-gated, free breathing; $NG_D$ - non-gated, deep breathing. . . . .	60